



Master Thesis

Deformation induced microstructure evolution during dynamic and static recovery in AA6061 aluminium alloys

carried out for the purpose of obtaining the degree of Dipl.-Ing., submitted

at TU Wien, Faculty of Mechanical and Industrial Engineering, by

Bernhard Viernstein, BSc

Mat.Nr.: 1125308

under the supervision of

Univ.Prof. Dipl.-Ing. Dr. techn. Ernst Kozeschnik

and

Univ.Ass. Dipl.-Ing. Johannes Kreyca

Institute of Materials Science and Technology, E308

Vienna, 12, 2017

Signature

Abstract

The substructure evolution of cold deformed AA6061 aluminium alloys is investigated during annealing processes at a temperature of 325 °C. The specimens are homogenized, quenched and artificially aged to ensure a homogeneous and stable distribution of precipitates in order to avoid precipitation hardening during further heat treatments. Annealing times vary between 5 seconds and 10^4 seconds, and the microstructural evolution is observed by using Electron Backscatter Diffraction (EBSD). Static recovery arises by a rearrangement of dislocations to minimize the total energy, which can be detected by subgrain growth. The similitude principle correlates the subgrain diameter to the average dislocation density, ensuring a comparability to predictive models, such as the extended Kocks-Mecking model. The advantage of this method is the additionally gained information about the arrangement of dislocations and the associated description of the microstructure.

Kurzfassung

Um den steigenden Materialanforderungen gerecht zu werden, ist die Kenntnis der mechanischen Werkstoffeigenschaften wie Festigkeit, Härte, Duktilität und Zähigkeit unabdingbar. Hierbei spielen Kristalldefekte, wie Versetzungen, eine entscheidende Rolle, da deren Bewegungen durch das Material die Grundlage der plastischen Verformung darstellen. Ziel dieser Arbeit ist die Beschreibung der Substrukturentwicklung von kaltverformten AA6061-Aluminiumlegierungen während einer Wärmebehandlung bei 325 °C. Vor der Verformung werden die Proben zunächst lösungsgeglüht, abgeschreckt und warmausgelagert, damit gleichmäßig verteilte Ausscheidungen bereits stabil vorliegen und keine Ausscheidungshärtung bei weiteren Wärmebehandlungen zu erwarten ist. Die Mikrostruktur der zwischen 5 Sekunden und 10^4 Sekunden geglühten Proben wird dabei mittels EBSD Aufnahmen beschrieben. Die hervorgerufene Erholung des Gefüges wird durch eine energetisch günstigere Anordnung der Versetzungen realisiert, welche sich durch ein Subkornwachstum äußert. Mittels des Similitude Prinzips kann eine Verknüpfung des Subkordurchmessers mit einer durchschnittlichen Versetzungsdichte hergestellt und mit Modellen, wie dem erweiterten Kocks-Mecking-Modell, verglichen werden. Der Vorteil dieser Herangehensweise ist der zusätzliche Informationsgewinn über die Versetzungsanordnung und der damit verbundenen Beschreibung der Mikrostruktur.

Acknowledgement

I would like to express my gratitude to Prof. Dr. Ernst Kozeschnik, for giving me the opportunity to be a member of his team and for helping me to realize this master thesis at the Institute of Materials Science and Technology. Special thanks go to Dipl.-Ing. Johannes Kreyca for his enduring and enthusiastic guidance through this project. Without his great encouragement, this master thesis would not have been possible.

The Materials Center Leoben Forschung GmbH is gratefully acknowledged for financial support.

I am particularly indebted to: Tomasz Wojcik for the EBSD investigations and for helpful advice regarding the use of OIM, Kurt Caloun for his dedicated support in experimental set ups; Thomas Weisz and Heinrich Buken for sharing their knowledge as well as Edith Asiemo and Christian Zaruba for supporting me in the laboratory.

Generally, I would like to express my appreciation to the entire workgroup for supporting me in various respects and for the pleasant working atmosphere.

Alexander, Johanna, Maxi and Consti, thank you for your lifelong friendship. You accompany and support me in all kinds of situations aside from university. I am glad we go through thick and thin and to have you by my side for so many years.

My best thanks go to my parents for all of their support in numerous ways during my studies and to my brother, for giving me advice in chemical matters every now and then. Pia deserves special thanks for proofreading on the one hand, and her enormous patience on the other hand.

Table of contents

1 Introduction	1
2 Objectives	2
3 State of the art.....	3
3.1 Crystalline structure	3
3.2 Crystal defects	5
3.2.1 Zero-dimensional defect (point defect)	5
3.2.2 One-dimensional defect (line defect).....	5
3.2.3 Two-dimensional defect (plane defect)	8
3.2.4 Three-dimensional defect (volume defect).....	9
3.3 Experimental observations	9
3.3.1 Electron Backscatter Diffraction (EBSD)	10
3.3.2 Subgrain structure	11
3.3.3 State parameter	14
3.4 Work hardening	17
3.5 Hardness tests	19
3.6 Scaling laws	20
3.7 Extended Kocks-Mecking approach	21
4 Experimental Part	23
4.1 Sample preparation	23
4.2 Temper state.....	23
4.3 Deformation experiments.....	25
4.4 Heat treatment	26
4.5 Hardness tests	27
4.6 EBSD	27
4.7 Data preparation	28
4.7.1 Grain definition	28
4.7.2 Kernel Average Misorientation (KAM).....	29
4.7.3 Clean up methods and filters.....	30
4.7.4 Subgrain characterization	31
5 Results	32
5.1 Simulation	32
5.2 Hardness tests	33

5.3 EBSD investigations	34
5.3.1 Deformation state: $\varphi = 0.7$; annealing time: none	35
5.3.2 Deformation state: $\varphi = 0.7$; annealing time: 150 sec.....	36
5.3.3 Deformation state: $\varphi = 0.7$; annealing time: 700 sec.....	38
5.3.4 Deformation state: $\varphi = 0.4$; annealing time: none	39
5.3.5 Deformation state: $\varphi = 0.4$; annealing time: 3.000 sec.....	40
5.3.6 Deformation state: $\varphi = 0.4$; annealing time: 10.000 sec.....	42
5.3.7 Compilation of experimental results	43
6 Discussion	45
7 Summary and Conclusion.....	50
8 References	51
9 List of figures.....	55
10 List of tables.....	58
11 Appendix	59

1 Introduction

The understanding of strengthening mechanisms is of paramount importance due to their omnipresence in industrial fields. Since work hardening, precipitation hardening and solution hardening are based on a hindered motion of dislocations, the arrangement and interaction of dislocations within the material is decisive. In order to reduce internal stresses after plastic deformations, heat treatments are conducted either to induce recovery or recrystallization processes. The resulting microstructural evolution is crucial for understanding the underlying mechanisms, leading to intense scientific research related to this topic.

This thesis focuses on the generation and annihilation of dislocations during cold deformation and subsequent annealing processes. Hence, the microstructure is characterized by the average dislocation density, and an extended Kocks-Mecking one-parameter model is applied. By this approach, the evolution of the dislocation density during dynamic and static recovery is calculated. The fitting parameters for dynamic recovery are determined by the obtained flow curves. During deformation processes, dislocations arrange in energetic favourable states, leading to a typical substructure formation. Cell-blocks are detected by Electron Backscatter Diffraction (EBSD) investigations. Substructure boundaries are generated by the accumulation of dislocations and cause an orientation change, which can be measured. The characteristic distances between these boundaries are related to the average dislocation density by the empiric similitude principle. During static recovery, subgrain coarsening occurs and the increase of the characteristic length is related to the reduction of the dislocation density. These experimentally obtained dislocation density values are in good agreement to those modelled with the extended Kocks-Mecking approach.

The softening behaviour during the annealing process is characterized by hardness tests. The decrease of the Brinell values with ongoing annealing time is linear on semi-logarithmic scale for recovery mechanisms. The onset of recrystallization occurs after annealing for 10^4 seconds at a temperature of 325 °C, but does not reflect in the hardness values.

2 Objectives

The major objective of the present work is to find appropriate state parameters for the microstructural characterization during annealing processes. For this purpose, the misorientation of low angle boundaries, subgrain diameters, as well as dislocation densities are taken in consideration. The reliability of obtained dislocation densities is determined by predictive models. The impact of subgrain growth in terms of dislocation density is investigated. A further objective is to relate the specimens' hardness to recovery processes.

3 State of the art

This chapter describes the fundamental background of crystallographic structures, including the periodic arrangement of atoms and existing crystal defects. Both, the motion of dislocations due to applied stress and the resulting plastic deformation as well as recovery processes during cold deformation are explained. Arising substructures with characterizing parameters, such as misorientations and subgrain sizes, are introduced to specify Electron Backscatter Diffraction (EBSD) maps after various heat treatments. Subsequently, numerous deformation modes are described on a macroscopic scale and flow curves are characterized by a subdivision into their four typical stages. Scaling laws are introduced, generating a correlation between applied stresses and state parameters, which describe the microstructure. At the end of this chapter, the extended one-parameter Kocks-Mecking model is explained, due to its ability to model the measured evolution of dislocation density during cold deformation and subsequent annealing processes.

3.1 Crystalline structure

Solid materials can be classified according to the regularity of the atoms' arrangement. Within crystalline materials, a long-range order exists, which is absent in noncrystalline or amorphous materials. A single crystal is defined, if a periodic structure extends throughout the entire specimen without interruption, whereas polycrystalline materials are composed of grains with random crystallographic orientations. The arrangement of atoms within metals is of periodic nature and each atom position is defined by the translation vector T , using the following linear combination [1]

$$\vec{T} = m_1 * \vec{a} + m_2 * \vec{b} + m_3 * \vec{c} \quad (1)$$

The basis vectors $a = \overrightarrow{OA}$, $b = \overrightarrow{OB}$ and $c = \overrightarrow{OC}$ have magnitudes equal to the lattice parameters, and are shown in Figure 1 [2]. These vectors form a parallelepiped with $\alpha = \angle BOC$, $\beta = \angle AOC$ and $\gamma = \angle AOB$, which is called a unit cell. The geometrical information of the crystalline structure is determined by the shape and size of the unit cell.

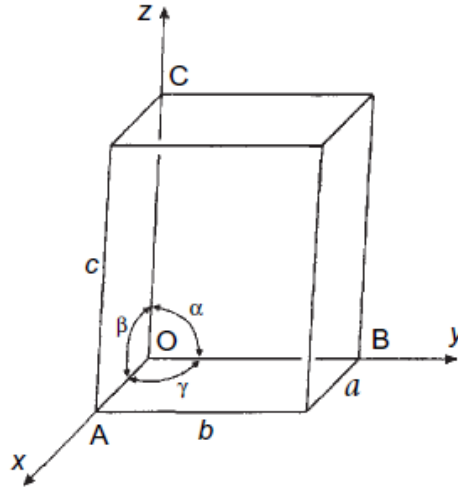


Figure 1: Unit cell with basis vectors a, b and c [3]

By varying the lattice parameters and/or the angles α , β , γ , seven crystalline systems can be distinguished. Furthermore, 14 Bravais lattices are defined, depending on the particular atom positions. Aluminium has a face-centered cubic structure (fcc) with $|a| = |b| = |c|$ and $\alpha = \beta = \gamma = 90^\circ$. The atoms are located at the corners of the unit cell and in the middle of each cubic face. Therefore, in total four atoms belong to a unit cell, leading to a packing density PD of 74%. Other typical crystal structures are body centred cubic (e.g. Tungsten, Molybdenum) and hexagonal close-packed structures (Graphite, Magnesium), but they are not taken into account in this work. Lattice planes are described by using Miller indices (hkl). The intersection points A, B and C in Figure 2 are represented in terms of basis vectors a, b, c: $\vec{OA} = m_1 * a$, $\vec{OB} = m_2 * b$ and $\vec{OC} = m_3 * c$. Miller indices are calculated in following Eqs.:

$$h = \frac{p}{m_1}; k = \frac{p}{m_2}; l = \frac{p}{m_3}, \quad (2)$$

where p symbolizes the least common multiple of the scalars m_1 , m_2 and m_3 .

Many mechanical properties are based on the interaction of dislocations. Therefore, the dislocation density ρ counts the amount of dislocations per area, which can be done experimentally, or states the length of all dislocations within a reference volume. Cold deformation of aluminium alloys leads to $\rho \sim 10^{13} - 10^{14} \text{ m}^{-2}$.

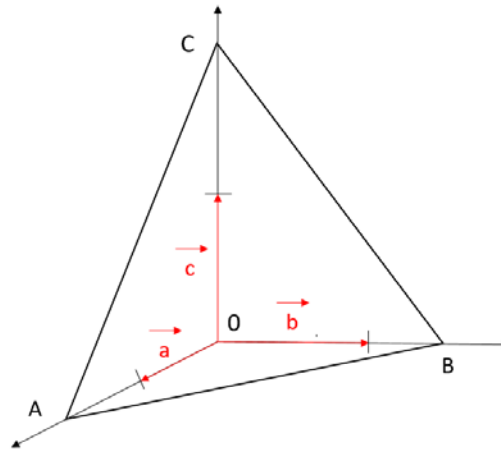


Figure 2: Lattice plane intersecting the coordinate system

3.2 Crystal defects

Under real circumstances, crystals contain defects. The periodic arrangement of atoms can be disturbed by a couple of different imperfections and will be discussed in the following sections.

3.2.1 Zero-dimensional defect (point defect)

Point defects arise if atoms are not positioned at their designated atom sites. The remaining zone of a removed atom is called vacancy (= Schottky defect) [1]. Interstitial atoms are located on non-lattice sites and are called *intrinsic defects* if all atoms are identical, or *extrinsic defects* if impurity atoms are involved. A substitutional atom replaces an atom of the parent lattice [3]. The size difference of a solute and a solvent atom does not exceed 15%, otherwise the solute atoms create substantial lattice distortion and a new phase will form [4].

3.2.2 One-dimensional defect (line defect)

One-dimensional defects are caused by a lattice distortion along a line. These defects are called dislocations and the occurrence of plastic strain during deformation is explained by the defects' motion through the crystal. The focus of this thesis lays on the description of the arrangement of dislocations during annealing processes; therefore, this chapter will briefly describe the theoretical background of these one-dimensional defects.

In the 1930s, the concept of dislocations was developed to describe plastic deformation within a crystal. This invention got necessary due to the inability to explain plastic deformation by theoretical calculations. The theoretical shear stress is several orders greater than observed

values [5]. In the 1950s, the existence of dislocations was proofed with electron microscopy. Since then, dislocations are considered the basis of many physical and mechanical properties. Two different kinds of dislocations can be distinguished: edge dislocation and screw dislocation.

Edge dislocations cause a local lattice distortion at the end of an additional half-plane of atoms, which is called dislocation line. An edge dislocation, as shown in Figure 3, is forced in x-direction, if a shear stress is applied in a direction perpendicular to the dislocation line. If no obstacle prevents further motion, an edge on the crystal's surface is established, which is one atomic distance wide [4].

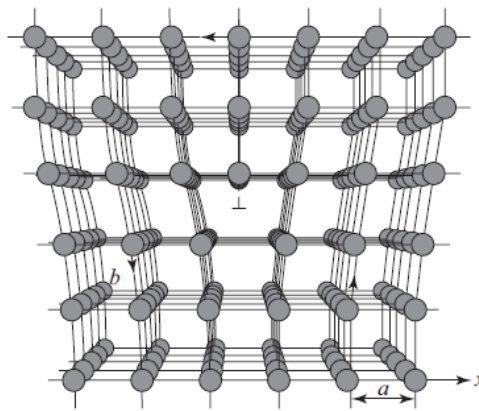


Figure 3: Additional half-plane of atoms causing an edge dislocation; a is the atomic distance [4]

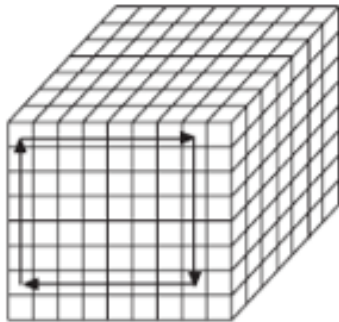
Atoms directly above the dislocation line are squeezed together, resulting in a compression field, whereas tensile stresses are induced in areas beneath the end of the half-plane of atoms. Consequently, dislocations of the same sign and identical slip plane, mutually push each other away. Dislocations of opposite sign are attracted to each other and annihilate in case of encounter. As a result, two additional half-planes combine and become a complete plane.

The existence of stress fields demands energy input and for edge dislocations the line energy approximately yields $\Gamma_{\S} = \frac{1}{2}Gb^2$, whereas $\Gamma_{\perp} = \frac{3}{2}\Gamma_{\S}$ for screw dislocations; G is the shear modulus and b defines the Burgers vector [6].

A Burgers vector b describes the magnitude and direction of the lattice distortion [4]. This dislocation displacement vector is described with reference to Figure 4. Figure 4a shows a perfect reference lattice, including a closed, clockwise Burger circuit represented by four arrows. The right side depicts the same circuit within a crystal containing an additional half-plane of atoms. In order to close the circuit, the Burgers vector b is required. Hence, b is

perpendicular to the dislocation line and parallel to the applied shear stress, which is only valid for edge dislocations.

(a)



(b)

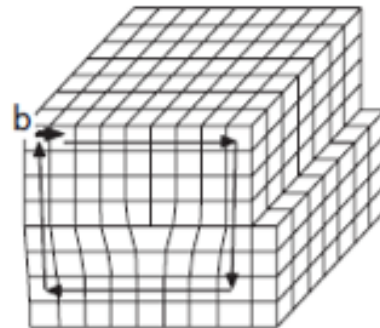


Figure 4: (a) Burgers circuit in a perfect lattice; (b) lattice with an included half-plane; b defines the Burgers vector [4]

Screw dislocations arise from shearing a part of the lattice of atoms. Comparable to edge dislocations, a screw dislocation line indicates a distortion caused by the crystal defect. By defining a Burger circuit in the distorted lattice, the Burgers vector that is required to close the same circuit in a perfect reference lattice is parallel to the dislocation line. The spiral or helical path of the Burger circuit coins the name of screw dislocations.

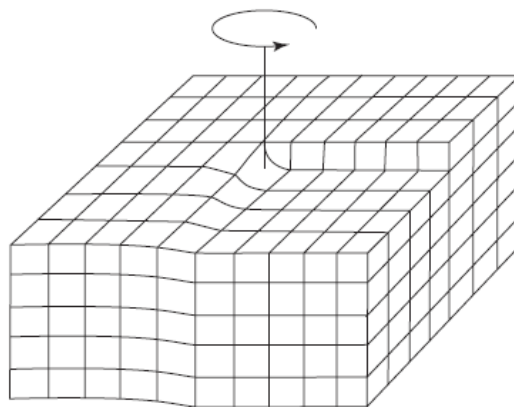


Figure 5: Screw dislocation [4]

The crystal structure specifies the direction of dislocation motion. Preferred lattice planes for slip processes are called slip planes, and together with a possible slip direction, a slip system is defined. A slip plane is given by the densest packed plane. Slip directions correspond to the direction of the lowest atom distances. For fcc metals, four slip planes, each containing three slip directions, are possible, stated by $\{111\} \langle 1\bar{1}0 \rangle$. If an obstacle prevents further motion, screw dislocations can change the slip plane in case the other slip plane contains the direction

of the Burgers vector. This so called cross slip does not exist for edge dislocations. Another method for bypassing obstacles is called climbing. Atoms of the additional half-plane of edge dislocations diffuse to vacancies and therefore elevated temperatures are necessary. The resulting glide plane is parallel to the original one.

As already mentioned, applied shear stress is responsible for sliding processes. For a single crystal Eq. (3) calculates resolved shear stresses τ_R if tensile or compression stresses σ are applied [4].

$$\tau_R = \sigma \cos \phi * \cos \lambda \quad (3)$$

ϕ is the angle between the normal to the slip plane and the direction of stress; λ represents the angle between the gliding direction and σ . One slip system is favoured due to a maximum value of $\cos \phi * \cos \lambda$ (Schmid factor) leading to the highest resolved shear stress. Dislocation motion starts if τ_R exceeds the critical resolved shear stress τ_{crss} . Therefore, the necessary initiated stress for plastic deformation (σ_y) is given by:

$$\sigma_y = \frac{\tau_{crss}}{(\cos \phi * \cos \lambda)_{max}} \quad (4)$$

The material state parameter σ_y is called “yield strength”. In polycrystalline materials, the Taylor factor M is introduced to relate the macroscopic flow stress σ to the acting shear stress τ in the slip systems on the one hand, and the macroscopically imposed strain ϵ to the total slip on all glide systems in the grain $\Sigma \gamma$ on the other hand [7].

3.2.3 Two-dimensional defect (plane defect)

A specific array of layers which stack on each other, characterizes a perfect crystal structure. The stacking sequence of perfect fcc structures is ABCABC... Two-dimensional defects break up this order by inserting a new lattice plane leading to a sequence of ABCBABC, for instance. This is called extrinsic defect, while intrinsic defects are defined as a partly removal of an existing plane [3].

Beside stacking faults, surfaces, grain boundaries and phase boundaries are considered as two-dimensional defects. Surfaces of solids restrict the crystalline structure and surface atoms occupy a higher energy level than bulk atoms, based on the lowered coordination number. Polycrystalline materials consist of randomly orientated grains, which are separated through

grain boundaries. These two-dimensional defects are called low angle boundaries if the misorientation θ of the grains is smaller than 15° , and high angle boundaries if $\theta > 15^\circ$. Figure 6 shows one possibility of a low angle boundary generation by a sequence of edge dislocations.

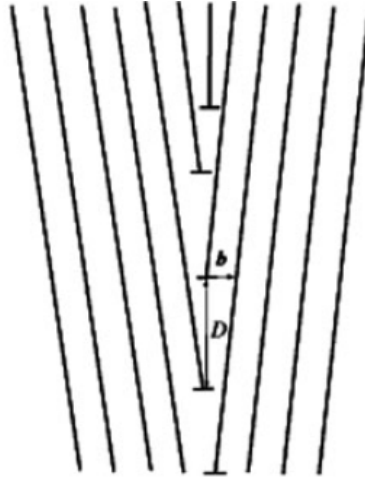


Figure 6: Misorientation based on edge dislocation; b is the Burgers vector, D the dislocation spacing [8]

3.2.4 Three-dimensional defect (volume defect)

Beside previously discussed defects, three-dimensional defects influence mechanical properties of the material. Volume defects are widely extended and may occur during the material's manufacturing process. Precipitates, inclusions, pores and cracks are examples of volume defects. They are not further considered in this thesis, because they are supposed to be constant due to previous heat treatments (see section 4.4)

3.3 Experimental observations

Microstructural analysis is the basis for understanding material properties. Many methods are available, but the most accurate method for analysis at the subgrain/grain level is given by Electron Backscatter Diffraction (EBSD) [10, 11]. Many thousands of grains and subgrains can be characterized from a single map by rapid and automated acquisition and analysis of the diffraction patterns [9]. Though the magnification of using Transmission Electron Microscopy (TEM) is much higher, it is only possible to investigate small areas of the specimen and no representative picture of the material is obtained to be examined. Additionally, the preparation of specimen for TEM is more complex and the equipment is more expensive compared to EBSD measurements. The impossibility to image individual dislocations with

EBSD has no relevance, since subgrain diameters are used to characterize the microstructural evolution during recovery in this thesis.

3.3.1 Electron Backscatter Diffraction (EBSD)

With EBSD measurements, grain orientations, local texture, point to point orientation correlations, and phase distributions can be identified. The detector is part of a scanning electron microscope and is based on the measurement of backscattered electrons. A high energy electron beam is focused on the specimen, which is tilted 70° towards a CCD camera. Those backscattered electrons that fulfil the Bragg's law, interfere constructively and form visible bands on a phosphorus screen, as shown schematically in Figure 7a.

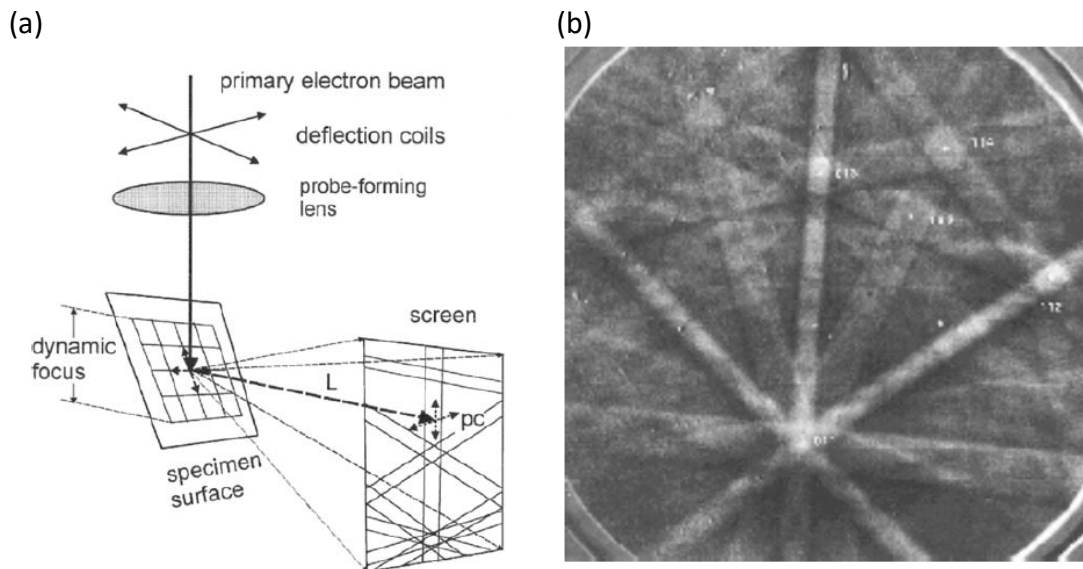


Figure 7: (a) Scheme of EBSD measurements [11]; (b) obtained Kikuchi bands [6]

EBSD patterns provide information about crystallographic orientations, which are represented by Kikuchi bands, as shown in Figure 7b. The width of the bands is inversely proportional to the interatomic spacings. Each band corresponds to a certain lattice plane and can be indexed by one specific set of Miller indices. Therefore, Triplet Indexing is used; interplanar angles of a triplet of bands are compared with a look-up table, relating angles with Miller indices. Each triplet of bands leads to an orientation solution and gets one vote. The most voted solution is the most probable one and is characterized by the confidence index (CI):

$$CI = \frac{V_1 - V_2}{V_{ideal}} \quad (5)$$

V_1 is the highest ranked solution, V_2 the second highest ranked solution and V_{ideal} the total number of votes. The confidence index is required due to the fact that multiple solutions can be found for a set of bands. Crystallographic orientation can be represented in an orientation map. Orientations are indicated by specific colours, which are given in an inverse pole figure beside the orientation map. Inverse pole figures are stereographic projections: normal vectors of selected crystallographic planes intersect a positive unit hemisphere in so called poles and are projected into two dimensions, as shown in Figure 8 [12].

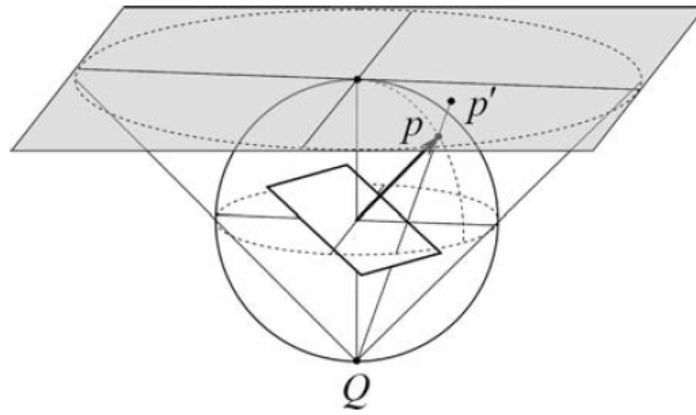
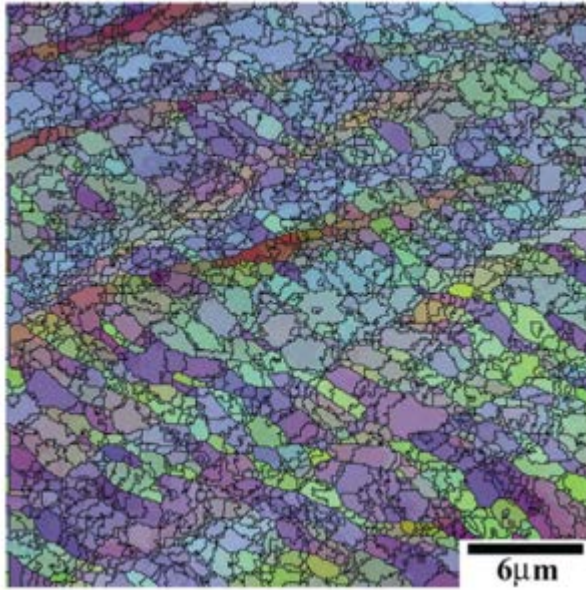


Figure 8: Point P indicates a crystallographic plane's orientation by a point on the surface of a sphere and P' is the stereographic projection onto a plane [12]

3.3.2 Subgrain structure

Recovery processes result in specific arrangements of dislocations based on the energy minimization principle. Dislocations can glide on slip planes, as described above, forming a regularly ordered microstructure while shear stresses are applied. Though Taylor's model requires five operating slip systems for homogenous plastic deformation, established surface observations [11, 12] proof that less independent slip systems are activated within individual parts of the grain. Fewer slip systems lead to a reduced number of intersecting jogs and are energetically favourable [15]. The reduced number of slip systems, which may depend on parameters like grain size, grain orientation, or on the deformation mode, subdivides a grain into cell-blocks, as shown in Figure 9a by an EBSD map and schematically in Figure 9b [16].

(a)



(b)

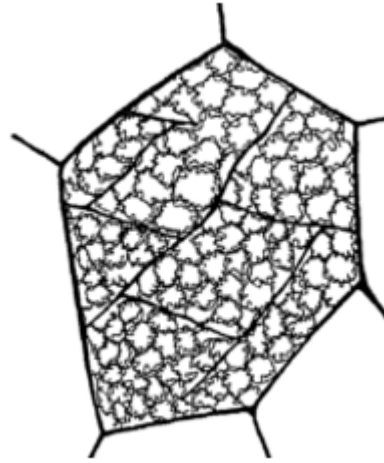


Figure 9: (a) EBSD map showing a typical substructure after 50% rolling of a high purity Al–0.13 wt% Mg DC cast alloy [17]; (b) schematic representation of cell-blocks within a grain [16]

Cell-blocks contain adjacent cells, which develop by the activation of the same combination of slip planes. Cell-blocks are delineated by dense dislocation walls (DDW) that are shown as thick lines within a grain in Figure 9b. The expression geometrically necessary dislocation (GND) is often used as a synonym for DDW, because they automatically arise when two cells-blocks with different orientations converge. Incidental dislocation boundaries (IDB) border individual cells and are formed by random trapping of mobile and stored dislocations. The misorientations of IDBs are much lower than of DDWs and increase much slower with deformation [18].

Figure 10 shows a transmission electron micrograph of pure Ni after a rolling reduction of 20%. A sketch in the top right corner symbolizes GNBs as solid lines and IDBs as speckled lines. Furthermore, the trace of the {111} slip planes, as well as the rolling direction RD are delineated.

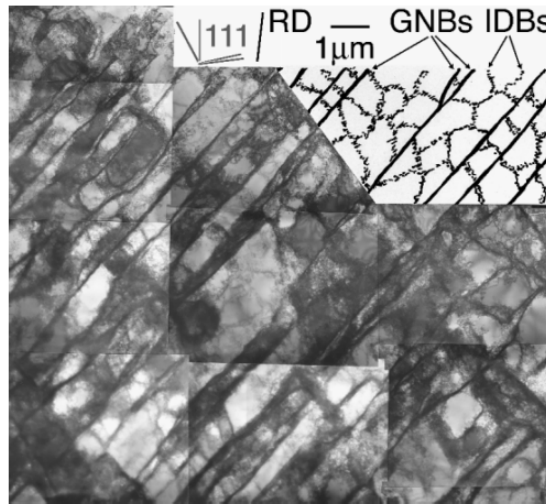


Figure 10: Transmission electron micrograph of deformed pure Ni; delineation of GNBs, IDBs and the rolling direction [14]

By further deformation, microbands (MBs) may occur. MBs are composed of small pancake-shaped cells and have a width of a few tenth of a micrometre. They contain a high dislocation density and appear to develop from DDW. Cells within MBs are formed by the activation of different glide systems compared to neighbouring CBs, and are partly supplied with dislocations that are previously stored in DDWs [13].

Figure 11 is similar to Figure 10, but almost all DDWs are extended to form MBs.

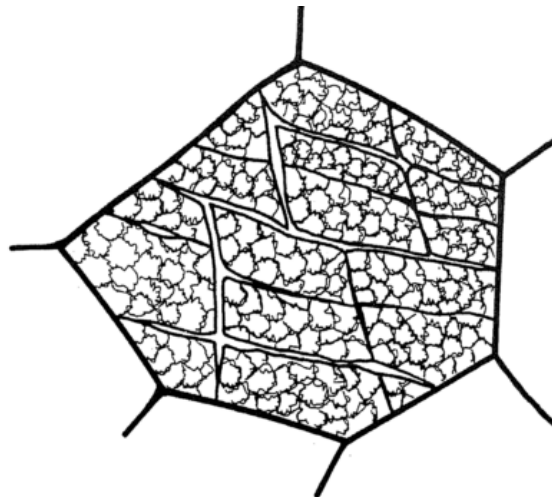


Figure 11: Cells within a grain subdivided by MBs [16]

Other features that may occur with increasing strain are microshear bands. These bands are caused by localized lattice rotations based on non-uniform strains. With increasing deformation, the angle of the microshear bands to the rolling plane decreases significantly, which is reasonably consistent with a rigid body rotation [17]. Examples for microshear bands,

realized as red structures, are illustrated in Figure 9a. These structures are composed of finer scaled cells, compared to the original elongated structures.

During recovery, dislocation motion occurs in order to reduce stored energy. The dislocation density ρ decreases due to annihilation processes and low angle boundaries are founded because of a new arrangement into ordered arrays. This configuration reduces internal strain energies by overlapping strain fields; as a consequence, cellular structures arise.

Recrystallization reduces the energy state by the formation of new strain-free grains with a low dislocation density. For recrystallization to occur, elevated temperatures are required since the process is based on diffusion. The recrystallization temperature depends on the amount of prior cold work and lays typically between one-third and one-half of the melting temperature. After the formation of a grain nuclei, grain growth reduces the total area of grain boundaries. The fraction of recrystallization is calculated by the Mehl Avrami-approach. For a more detailed explanation see [7, 8, 9].

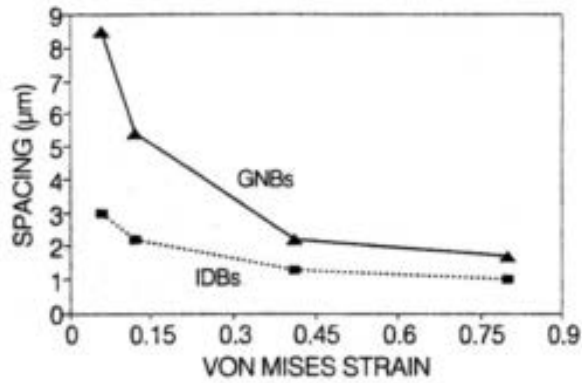
3.3.3 State parameter

The microstructural evolution during cold deformation can be described by state parameters. Therefore, the dislocation density, the misorientation angle of subgrain boundaries or the subgrain size, which is characterized by the boundary's spacing, are suitable. These parameters can be determined by EBSD investigations, with the exception of particular dislocations.

With increasing strain, the number of GNBs and MBs increases, leading to more intersections of these subgrain-boundaries. As a consequence, the size of ordinary cells decreases and the misorientation of their restricting structures increases. The distances between GNBs as well as the distances between IDBs heavily vary during deformation and are suitable parameters for microstructural observations. The relationship between strain and spacing is plotted in Figure 12a. Compared to the spacing of IDBs, cell-blocks which correlate with the spacing of GNBs, are larger, yet the size decreases more rapidly at low strains. Differences between GNBs and IDBs diminish with strain and cell-blocks contract to one cell size width [22]. Subgrain boundaries divide adjacent areas that show slightly varying orientations. These misorientations can be measured by using OIM (see section 4.7), leading to relationships as plotted in Figure 12b. The average misorientation angles of high purity cold rolled aluminium and nickel are plotted for applied von Mises strain. The misorientation angle of IDBs is lower

and increases more slowly compared to GNBs.

(a)



(b)

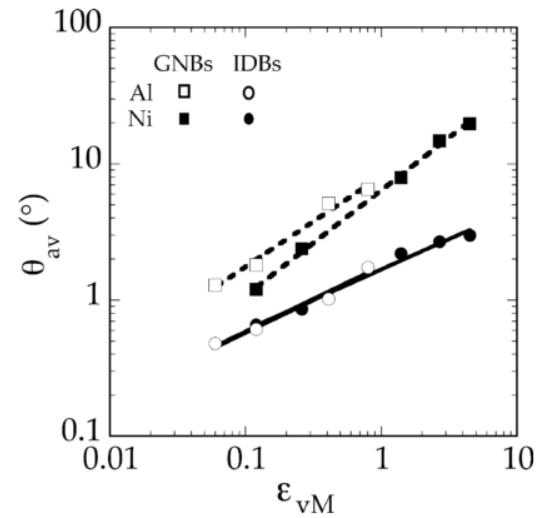
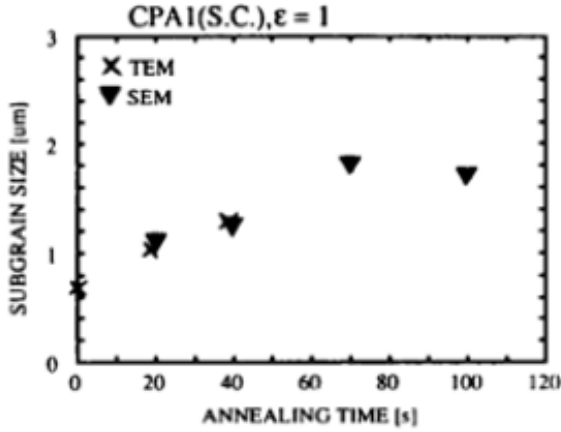


Figure 12: (a) Spacings [22] and (b) misorientation of GNBs and IDBs as function of strain [14]

The evolution of the subgrain size and the misorientation angle during static recovery have been investigated by several authors. The results coincide regarding the correlation between subgrain size and annealing time. With continuing annealing time, the mean subgrain size increases, as shown in Figure 13a. The results in Figure 13b clearly demonstrate that the average subboundary misorientation increases with increasing annealing time [23]. High purity Al0.43 wt% Fe0.09 wt% Si alloys are cold rolled to $\epsilon = 1$ and subsequently annealed at a temperature of 325 °C. A comparison of misorientations and the subgrain sizes obtained by an EBSD-technique and a convergent beam technique in TEM shows a good agreement of these methods. Furu and Nes [23] explain the increasing misorientation angle during static recovery with the existence of orientation gradients. In contrast, Huang and Humphreys [24] measured a slightly decreasing mean subgrain misorientation during annealing in the absence of orientation gradients within the sample. However, local strain gradients or “local lattice curvature” are characteristic features of most deformed grains.

(a)



(b)

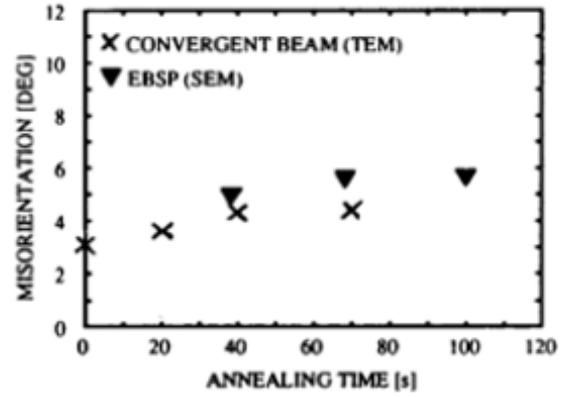


Figure 13: (a) Subgrain size as a function of annealing time; (b) misorientation as a function of annealing time

The stored energy after cold deformation and subsequent recovery annealing can be described by the average subgrain size δ and the boundary misorientation θ . The Read-Schockley relation correlates the sub-boundary energy γ_{SB} and the sub-boundary misorientation θ of the form

$$\gamma_{SB} = \alpha G b \theta \left(\ln \frac{e \theta_c}{\theta} \right), \quad (6)$$

where a common estimate for the θ_c value is 15° [23]. By increasing misorientation during annealing processes, the average subgrain energy increases during subgrain growth, but the total stored energy per unit volume P_D decreases due to the reduction of the total boundary area per unit volume λ [23].

$$P_D = \lambda \gamma_{SB} \text{ with } \lambda = \frac{\kappa_1}{\delta} \quad (7), (8)$$

κ_1 is a geometrical constant. A driving force exists if subgrain growth is accompanied by a reduction of P_D

$$F_D = -\frac{\partial P_D}{\partial \delta} = -\kappa \frac{\partial}{\partial \delta} \left(\frac{\gamma_{SB}}{\delta} \right) \quad (9)$$

The Einstein relation ($M = v/P$) defines the mobility of a boundary (M), which migrates with a constant velocity (v) due to a driving pressure (P) [23]. Since boundary motion is based on climbing processes in this approach, the mobility's temperature-dependency is given by bulk diffusion. T. Furu et al. (1994) point out that the subboundary speed increases with decreasing

boundary misorientation, confirmed by experimental observations [23].

3.4 Work hardening

Mechanical properties of metals are strongly influenced by the motion of dislocations. Several strengthening mechanisms are based on the interaction of these one-dimensional defects with the local structure. Dislocation glide can be prevented by trapping, traced on solutes, precipitates, grain boundaries or other dislocations. If an increasing amount of dislocations get stuck during deformation, it is called strain hardening. As a consequence, enhanced energy input is necessary to achieve further deformation. Deformations beneath the recrystallization temperature (often defined as 0.4 times melting temperature T_m) are called cold working or cold rolling, while the terms hot deformation or creep refer to deformations at higher temperatures ($>0.4 \cdot T_m$).

Generally, applied stresses cause macroscopic shape changes of metals. The impact on the microstructure strongly depends on the mode of deformation. The rate of increase of the grain boundary area per unit volume (S_v) as a function of true strain is shown in Figure 14, assuming an initial cubic grain of size D_0 .

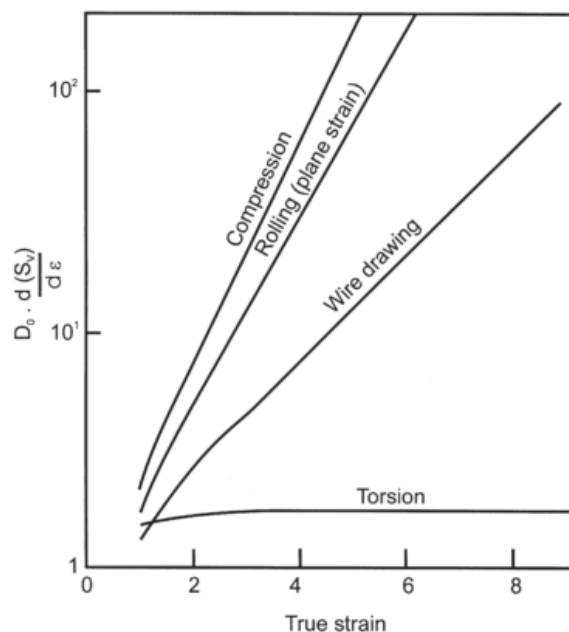


Figure 14: Rate of grain boundary growth per unit volume S_v for different modes of deformation [21]

There are various modes of deformation. Through rolling, the shape of grains becomes laths; by wire drawing, the grains become needles; and the grains of a compressed specimen are

disc shaped [21]. Furthermore, while necking occurs during tensile tests, barrelling takes place during compression tests. Inhomogeneous compression over the specimen's cross section is caused by friction effects and results in a deformation cross, expressing the largest deformation in X-configuration. Most-strained regions are in the centre and on the edge of the cylinder. A FEM-predicted distribution of effective strain displays a typical deformation cross in Figure 15.

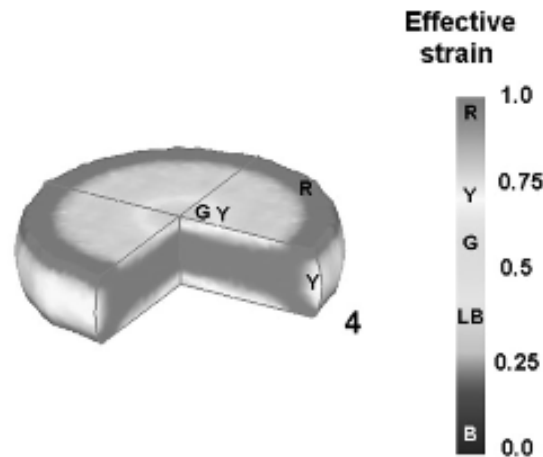


Figure 15: FEM-predicted distribution of effective strain in hot compression of Al cylinder [25]

To reduce friction effects, lubricants such as Graphite, or Molybdenum are used. During compression tests, the specimen's hardness increases, based on the hindered motion of dislocations. Work hardening affects the trend of stress-strain curves which can be classified into four stages. Plastic deformation in stage I is based on easy glide. Only one slip system is active and therefore pre-existing obstacles are the only restricting barriers for dislocation motion. By further deformation, additional slip planes get activated, leading to interactions of dislocations on intersecting slip planes. A linear strengthening rate defines stage II, which is only weakly sensitive to temperature and strain rate. Dynamic recovery starts in stage III, causing a decreasing hardening rate through annihilation processes [26]. Stage III strongly depends on temperature, leading to an increasing work hardening rate θ by decreasing deformation temperature for fcc metals and alloys in stage III [22].

In Figure 16a, schematic flow curves are plotted, including the subdivision into the stages II, III and IV, as described above. Since stage I strongly depends on the crystal orientation and does not occur if several slip systems are activated from the start, it is not considered in this figure. The transition of each stage is gradual and is distinguished more clearly in the Kocks-

Mecking diagram (Figure 16b), which displays the work hardening (θ) as a function of flow stress (τ).

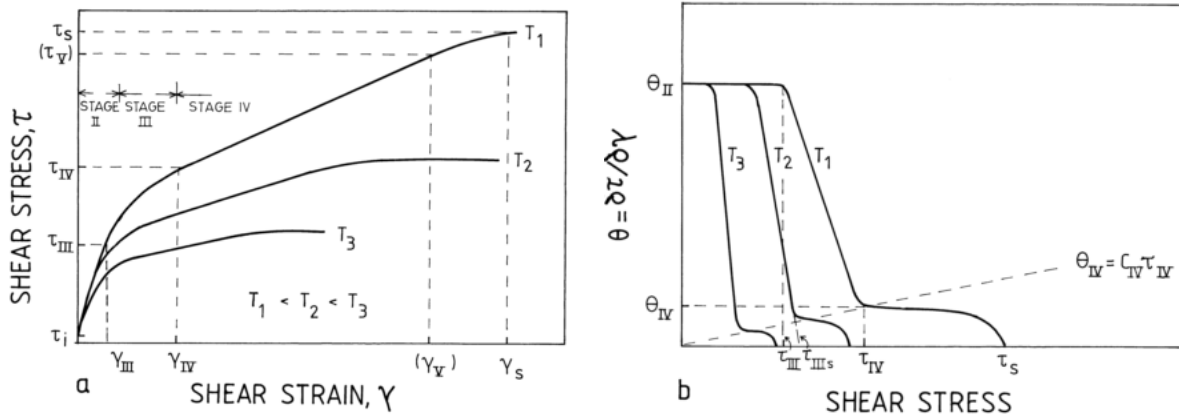


Figure 16: (a) Flow curve subdivided into stage II , stage III and stage IV; (b) Kocks-Mecking diagram visualizing strain hardening (θ) vs flow stress (τ) [26]

3.5 Hardness tests

Since work hardening and recovery processes directly influence the material's strength, hardness tests can be used for material characterizations. Hardness tests are inexpensive methods to evaluate the material's resistance to localized plastic deformation. A small indenter is forced into the specimen, and the depth and size of penetration is related to a hardness number. Different testing methods, such as Rockwell-, Vickers-, Brinell-, or Knoop-hardness tests are based on various shapes of indenters. For aluminium alloys, the Brinell hardness test is the method of choice.

In Brinell hardness tests, a spherical, hardened steel or tungsten carbide indenter is forced into the specimen's surface under constant load. Standard diameters of the indenter are 10 mm, 5 mm, 2.5 mm or 1 mm. The applied force F maintains constant for a specific time, to enable complete plastic deformation. Hardness is calculated by the diameter d of the remaining indentation and is given in Eq. (10).

$$HBW = \frac{0.102 \cdot 2 \cdot F}{\pi \cdot D \cdot (D - \sqrt{D^2 - d^2})} \quad (10)$$

D is the diameter of indenter; d is the diameter of remaining indentation. The value 0.102 converts Newton to the older unit Kilopond, in order to guarantee comparability to hardness tests in literature. For accurate results, a minimum distance of the centre of the indentation

to the edge of the specimen is defined as $2.5 * d$, as well as a minimum distance between adjacent indentations of $3 * d$ [4].

3.6 Scaling laws

Scaling laws relate two physical quantities that scale with each other over a significant interval. The Taylor equation and the similitude principle are two scaling laws used within this thesis. The former relates the flow stress of a material to the microstructure, namely the average dislocation density. The relation was introduced by G.I. Taylor to explain work hardening by dislocation generation, leading to enhanced stresses for continuing plastic deformation due to an increased glide resistance. The flow stress is assumed to be the external shear stress ($\tau \propto \frac{G*b}{r}$), which is required to force two dislocations on parallel glide planes to pass one another. Since the distance r of two dislocations is inversely proportional to $\sqrt{\rho}$, the Taylor equation states

$$\tau = \tau_0 + \alpha G b \sqrt{\rho} \quad \text{or} \quad \sigma = \sigma_0 + g_1 \sqrt{\rho}, \quad (11)$$

where α is called strengthening coefficient; the shear modulus G and Burgers vector b are scaling constants; τ_0 and σ_0 are the amount of stress that take strengthening mechanism without work hardening into account; and $g_1 = \alpha M G b$.

The similitude principle gives an empirical relationship between the flow stress τ and a characteristic wavelength d of dislocation patterns [27]. The relation is based on experimental observations [20, 21, 22] and no convincing explanation has been presented yet.

$$\tau = K \frac{\mu * b}{d} \quad (12)$$

K is the similitude coefficient; μ is the shear modulus; b is the Burgers vector and d is the characteristic wavelength of dislocation patterns. In reference to Kocks and Mecking [30], the similitude coefficient K is 7.5. The combination of the Taylor equation and the similitude principle yields

$$d = \frac{1}{\sqrt{\rho}} * \frac{K}{\alpha} \quad (13)$$

This Eq. is used to calculate the average dislocation density by measuring the characteristic distance d , which is determined to be the distance of GNBs in this thesis.

3.7 Extended Kocks-Mecking approach

To predict the dislocation density during deformation, a Kocks-Mecking - one parameter model is used [30]. The rate of dislocation storage is obtained by the balance of induced dislocations $d\rho^+/d\gamma$ and dislocation annihilations $d\rho^-/d\gamma$ during dynamic recovery [26].

$$\frac{d\rho}{d\gamma} = \frac{d\rho^+}{d\gamma} + \frac{d\rho^-}{d\gamma} = h_1\sqrt{\rho} - h_2\rho = \frac{M}{b \cdot A}\sqrt{\rho} - 2BM\frac{d_{crit}}{b}\rho, \quad (14)$$

where d_{crit} is the annihilation distance between two dislocations, and A and B are factors that need to be calibrated. The proportional factor A refers to the immobile dislocation production, when dislocations get stuck in front of an obstacle after moving an average mean free path. The increase of dislocation density is:

$$\frac{d\rho^+}{d\varepsilon} = \frac{M}{A \cdot b}\sqrt{\rho} \quad (15)$$

Factor B describes dynamic recovery at low and intermediate temperatures. Annihilation occurs when two dislocations of opposite sign get closer than d_{crit} and states

$$\frac{d\rho^-}{d\varepsilon} = 2 \cdot d_{crit} \cdot \rho \cdot B \cdot \frac{M}{b}, \quad (16)$$

A more detailed derivation of the dislocation generation and dislocation annihilation terms is presented in the Appendix. The parameters A and B are calibrated based on experimental results. A specific flow curve within the Kocks-Mecking framework is described by the yield stress σ_0 , the initial slope θ_0 and the saturation stress σ_∞ , which are shown schematically in Figure 17.

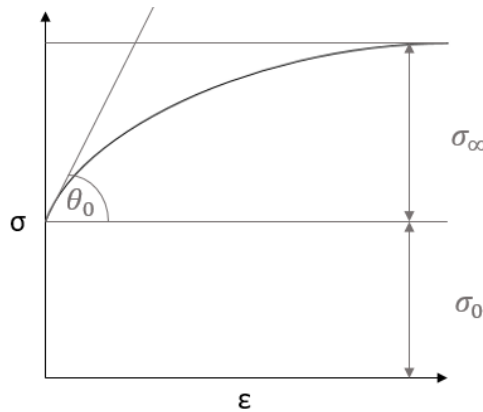


Figure 17: Description of σ_0 , θ_0 and σ_∞ for an unambiguous definition of a flow curve

The following Eqs. link the characteristic parameters σ_0 , θ_0 , σ_∞ with h_1 and h_2 :

$$\theta_0 = \frac{h_1 * g_1}{2} \quad (17)$$

$$\sigma_\infty = g_1 * \frac{h_1}{h_2} \quad (18)$$

With the knowledge of θ_0 and σ_∞ , h_1 and h_2 as well as the parameters A and B can be calculated. $\rho(\varepsilon)$ is calculated by solving the differential Eq. (14), and with the Taylor Eq. (11) [26] the stress contribution can be determined.

For elevated temperatures, the Kocks-Mecking approach is extended by an additional C parameter, which takes annihilation due to climbing processes into account. The C term states:

$$\frac{\partial \rho_s^-}{\partial \varepsilon} = -2CD_d \frac{Gb^3}{\dot{\varepsilon}kT} (\rho^2 - \rho_{equ}^2), \quad (19)$$

where $\partial \rho_s^- / \partial \varepsilon$ indicates a reduction of the dislocation density due to static recovery. ρ_{equ} is the equilibrium dislocation density, and $D_d = D_{d0} \exp(-Q_d/(RT))$ is the pipe diffusion coefficient. With $\frac{\partial \rho}{\partial \varepsilon} = \frac{\partial \rho}{\partial t} * \frac{\partial t}{\partial \varepsilon} = \frac{\partial \rho}{\partial t * \dot{\varepsilon}}$ the C term is independent of $\dot{\varepsilon}$ while considering $\frac{\partial \rho}{\partial t}$. The C term characterizes static recovery, because it is unequal zero for $\dot{\varepsilon} = 0$. This expression is of special interest in this thesis, since static recovery is investigated during annealing processes. In the present work, the C parameter is calibrated with experimentally derived evolution of the dislocation density (see section 6).

4 Experimental Part

In this thesis, deformed AA6061 specimens are analysed concerning microstructural constitution. This chapter describes the experimental procedure including heat treatments, compression tests, hardness tests, specimen preparation and EBSD investigations.

4.1 Sample preparation

The AA6061 alloys are industrially cast, homogenized and hot rolled. The chemical composition in weight percent is listed in Table 1.

Table 1: Chemical composition in wt% of AA6061 alloys

Al	Mg	Si	Fe	Ti	Cu	Mn	Zn	Cr	Ni	Pb	Ga	Residuals
97.35	0.85	0.69	0.45	0.05	0.23	0.11	0.05	0.18	0.01	0.01	<0.03	0.037

300 * 300 * 60 mm dimensioned AA6061 plates are shown in Figure 18, including the Rolling Direction (RD), the Transverse Direction (TD) and the Normal Direction (ND). Cylindrical specimens with a diameter of 10 mm and a length of 15 mm (see Figure 19) are extracted by spark erosion along the Normal Direction (ND).

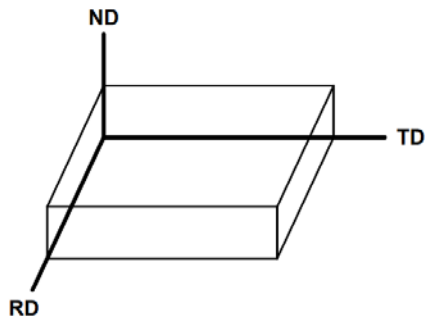


Figure 18: AA6061 plate

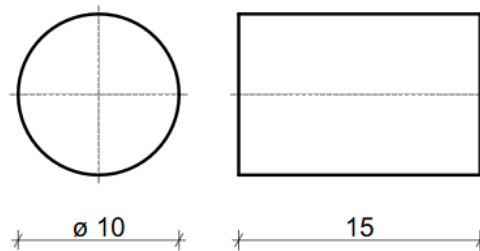


Figure 19: Dimension [mm] of the cylindrical specimen

4.2 Temper state

The cylindrical AA6061 specimens are heat-treated for one hour at 540 °C in a high temperature chamber furnace (HTF 1700) to guarantee the solution of the alloying elements

in the aluminium matrix. Subsequently, rapid water quenching produces a super saturated solution at room temperature. An artificial heat treatment for three hours at 350 °C generates stable, evenly distributed β' precipitates within the aluminium matrix.

Figure 20 schematically shows the heat treatment process, starting with a low heating rate of 270°/hour to prevent overshooting at a temperature of 540 °C. For the artificial aging process, the furnace is preheated up to 350 °C within one hour, before the specimen are placed in it.

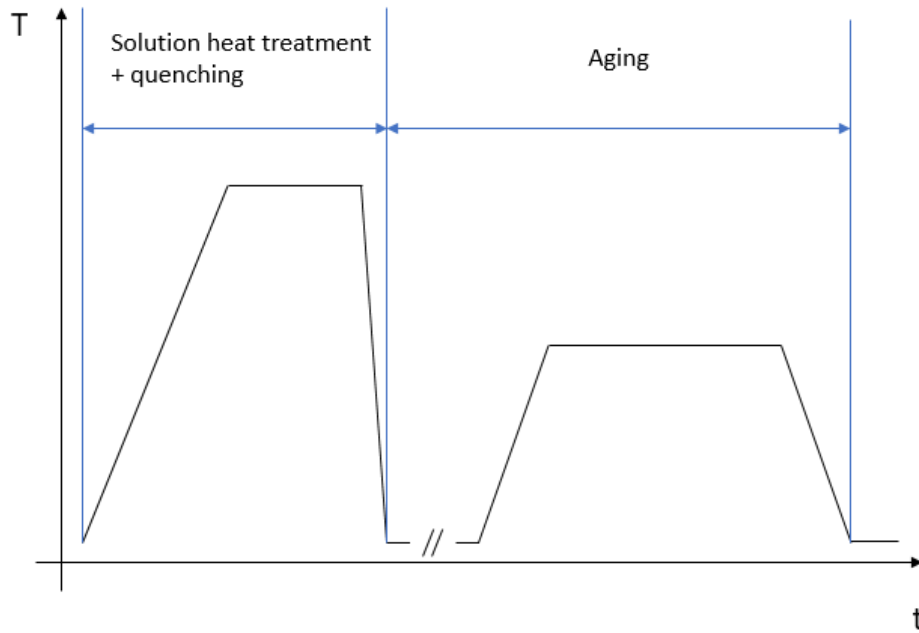


Figure 20: Scheme of heat treatment process

The heat treatment is simulated by the thermo-kinetic software package MatCalc (version 6.00 rel. 0.104) [31]. The databases *mc_al.tdb* [32] and *mc_al.ddb* [33] are used. These databases are available via the Open Database License [34], and can be downloaded for free from <http://matcalc.at>. The evolution of the phase fraction of GP-zones, β' and β'' precipitates are calculated to ensure the receipt of stable and evenly distributed precipitates and to exclude additional precipitation formation during further annealing processes at a temperature of 325 °C.

4.3 Deformation experiments

For the deformation tests, a servo hydraulic mechanical strain/compression testing machine (Gleeble 1500) is used. The cylindrical specimens are placed between two tungsten stamps, as shown in Figure 21.

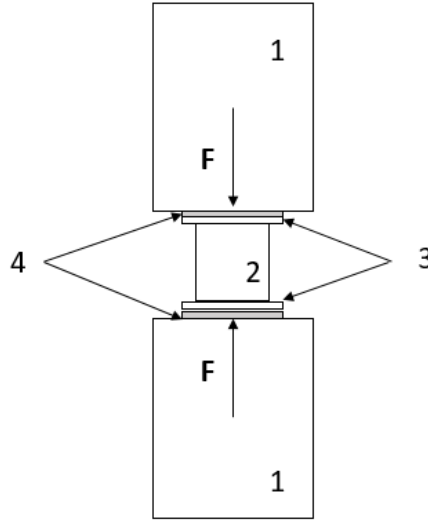


Figure 21: Schematic structure of Gleeble 1500; F: applied force; 1: tungsten stamps; 2: specimen; 3: molybdenum foil; 4: graphite foil

Molybdenum foils and Graphite foils (both 0.1 mm thick) prevent friction and ensure uniaxial compression tests without strong barrelling. Therefore, the effective area A during deformation yields: $A = \frac{V}{l}$, where V is the constant volume and l is the actual length of the cylinder. With this assumption, flow curves can be calculated with the obtained experimental data. All specimens are deformed with a constant strain rate $\dot{\varphi}$ of 0.01/sec. For achieving a final strain of $\varphi = 0.4$ and $\varphi = 0.7$, the deformation time results in 40 seconds and 70 seconds. Gleeble 1500 input parameters include the total deformation length ($\Sigma \Delta l$) and the associated deformation time (t_{Gleeble}), as listed in Table 2, due to the impossibility to adjust constant strain rates directly. Each time-value refers to the previous entry and is selected to be 5 seconds.

Δl is calculated by the following Eq.:

$$\varphi = \dot{\varphi} * t = \ln\left(\frac{l_0 + \Delta l}{l_0}\right) \rightarrow \Delta l = l_0 * e^{\dot{\varphi} t} - l_0 \quad (20)$$

Table 2: Calculated Gleeble input parameters

t [sec]	l(t) [mm]	$\varphi(t)$	Δl	$\Sigma(\Delta l)$	t_Gleeble[sec]
0	15	0	0	0	0
5	14,2684	0,05	-0,7316	-0,7316	5
10	13,5726	0,1	-0,6959	-1,4274	5
15	12,9106	0,15	-0,6619	-2,0894	5
20	12,2810	0,2	-0,6297	-2,7190	5
25	11,6820	0,25	-0,5989	-3,3180	5
30	11,1123	0,3	-0,5697	-3,8877	5
35	10,5703	0,35	-0,5420	-4,4297	5
40	10,0548	0,4	-0,5155	-4,9452	5
45	9,5644	0,45	-0,4904	-5,4356	5
50	9,0980	0,5	-0,4665	-5,9020	5
55	8,6542	0,55	-0,4437	-6,3458	5
60	8,2322	0,6	-0,4221	-6,7678	5
65	7,8307	0,65	-0,4015	-7,1693	5
70	7,4488	0,7	-0,3819	-7,5512	5

In total, 29 specimens are deformed to both $\varphi = 0.4$, and $\varphi = 0.7$, but five specimens are kept for the case of unexpected results.

4.4 Heat treatment

The dilatometer DIL 805 A/D is used for short annealing times up to 550 seconds, and the furnace Carbolite Type 3508 for annealing times longer than 550 seconds. This separation was based on the limited space within the induction coil in the dilatometer, permitting one treatment after the other. The heating rate is 65 °C/second and cooling is performed by He-gas, which streams against the specimens with a volume flow of 430 l/hour for 10 seconds. The furnace Carbolite Type 3508 is preheated to a temperature of 325 °C before the specimens are put in it, while the temperature stability is verified by a thermocouple. By removing the specimens for subsequent water quenching after a predefined time (compare Table 3), a temperature drop of approximately 5 °C is measured. EBSD investigations are accomplished after these annealing times, which are highlighted as bold numbers in Table 3.

Table 3: Annealing times for compressed specimens to $\varphi = 0.4$ and $\varphi = 0.7$

$\varphi = 0.4$	t [sec]	0	50	100	200	550	1000
		2000	3000	4000	5000	6000	10000
$\varphi = 0.7$	t [sec]	0	5	10	20	50	100
		150	200	250	350	550	700

4.5 Hardness tests

The deformed and heat-treated specimens need to be prepared for Brinell hardness tests, which are performed on the Emco Test M1C 010 machine. The specimens are cut by the Accuton-100 along the cylinder axis and are embedded, using the resin Araldite Ay 103-1 and the hardening agent REN HY 956. One half is used for hardness tests and the other one for selected EBSD investigations. The diameter of the Brinell sphere is 1 mm and the applied force is 5 kp (= 49.03 N), which corresponds to a possible hardness range of 16-110 HB. The distance between the edge of the specimens, as well as the distance between adjacent indentations is 1.5 mm, and is higher than 2.5 times the indentation diameter d . Figure 22 shows a scheme of the performed hardness tests.

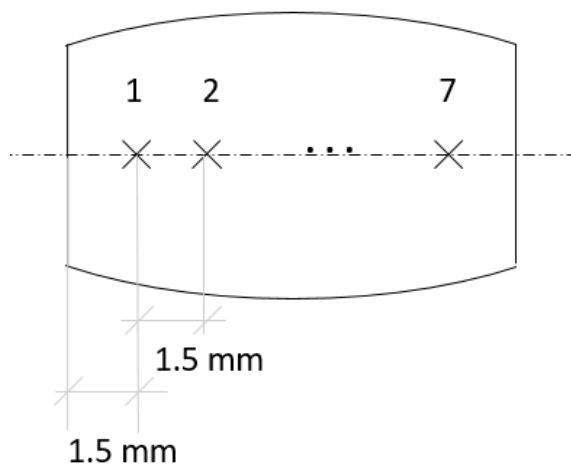


Figure 22: Schematic array for hardness tests

For each specimen, seven Brinell hardness tests are conducted along the specimen's centreline to detect the deformation states over the sample's cross section. Since all experiments are conducted twice, mean hardness values are calculated.

4.6 EBSD

Those specimen halves, which are not used for hardness tests, are embedded in a conductive mounting material CEM 3070 for EBSD investigations. In 2016, D. Sparber [35] improved the preparation technique for aluminium alloys, suggesting the following polishing and grinding steps [35]:

Table 4: Polishing and grinding steps [35]

Step	Polishing Disc	Grit [μm]	Time [min]	Step	Polishing Disc	Grit [μm]
Grinding	Abrasive Paper	500	2	Grinding	Abrasive Paper	500
Polishing	Struers MD Largo	9	15	Polishing	Struers MD Largo	9
Polishing	Struers MD Dur	6	25	Polishing	Struers MD Dur	6

The specimen and sample holder need to be cleaned in an ultrasonic bath between each step. A Colloidal Silica 50nm alkaline suspension is used for OPS. The OPS-step is followed by another polishing step, but instead of using the suspension, only ethanol, water and standard liquid soap are utilized. Subsequently, the specimen are cleaned in an ultrasonic ethanol bath, before the specimens are dried with a blow dryer [35]. The last preparation step, which is the removal of remaining residuals, is done by etching the specimens with a 5% hydrofluoric acid. Suggested etching times for industrial aluminium alloys are 15 seconds.

The structural investigations (EBSD) are carried out at USTEM on FEI Quanta 250 FEGSEM, using a back scattered electron detector as well as an OIM System with high speed Hikari CCD EBSD Camera and integrated Forward Scatter Detector. The acceleration voltage of electrons is 15 kV, and the adjusted step size is 0.2 μm , while an area of 66 μm x 120 μm is scanned.

4.7 Data preparation

This chapter depicts the functionality of Orientation Imaging Microscopy (OIM) (EDAX Inc.), an analysing technique for the identification of crystallographic structures, and it introduces clean up and filter methods to diminish mapping errors. OIM indexes EBSD patterns automatically and provides information in form of charts, highlightings or maps. OIM is a powerful technique to visualize the microstructure, but many parameters have to be set by the user. The following paragraphs describe essential definitions to avoid possible mistakes when using OIM.

4.7.1 Grain definition

For defining a grain, adjoining pixels are evaluated with respect to orientations. They are considered as two grains if the misorientation exceeds a tolerance angle, which is defined by

the user. This approach can lead to a large grain orientation spread, while the point to point misorientation keeps low. Additionally, a minimum grain size defines the minimum amount of pixels contributing to a grain. The tolerance angle was set to 4°, while at least eight pixels are required to form a grain. The following screenshot in Figure 23 shows these settings in OIM, which can be found at *Properties – Grain Size*:

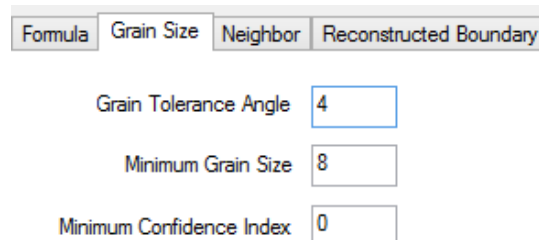


Figure 23: Screenshot of the settings, defining a grain in OIM

4.7.2 Kernel Average Misorientation (KAM)

In this mode, the misorientations between a pixel at a centre of a kernel and all points at the perimeter of the kernel are measured. The average misorientation value is assigned to the centre point. Those values, which exceed a defined tolerance angle are excluded. KAM-maps are used beside Auto IPF (Inverse Pole Figure) maps to identify subgrains. Figure 24 guides how to adjust the settings:

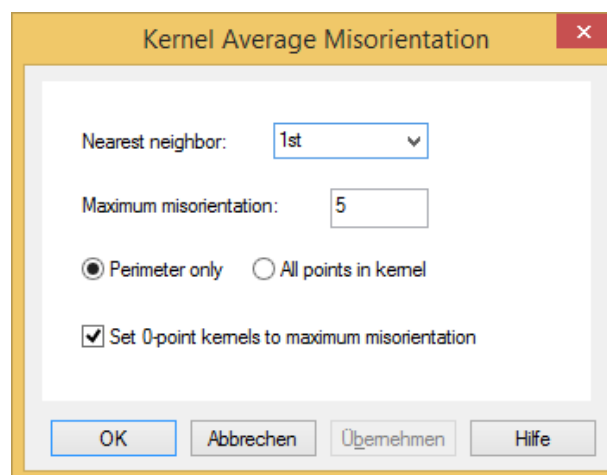


Figure 24: Guidance how adjust the settings to create a Kernel Misorientation map

4.7.3 Clean up methods and filters

Clean up methods and filters clear data to diminish mapping errors. Various clean up types are available, as listed in Figure 25. Grain Confidence Index Standardization, Grain Dilation and Kernel Smoothing are used and are therefore described in the following paragraphs.

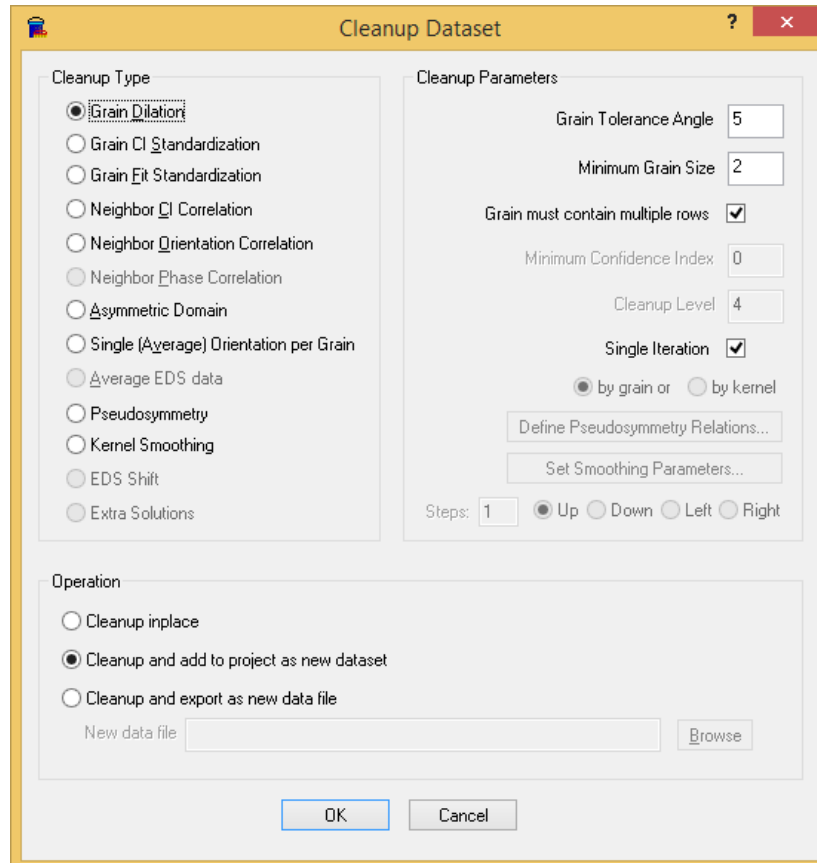


Figure 25: Clean up types including the clean up parameters, which can be selected by the user

Confidence index standardization (CIF) recovers low confidence indices that represent correct orientation measurements. CIF averages the confidence index of all pixels within a defined grain and it is recommended to be used since no orientations are changed.

If a pixel is not indexed or does not belong to any grain, the iterative clean up method *grain dilation* acts on this point. The particular pixel assumes the orientation of the majority of neighbours that belong to the same grain. Figure 26 describes this method.

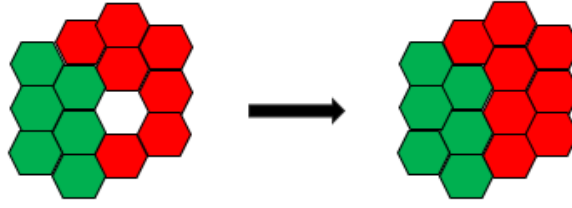


Figure 26: Grain dilation

The *Kuwahara filter* minimizes the spectrum of noise of the images, to identify IDBs of low misorientation. The pixel of interest is centred within a neighbourhood, whereas the adjusted size is set by the amount of nearest neighbours in the hexagonal grid. The number is set to one, defining the surrounding six pixels of the considered position. This hexagonal kernel is divided into six triangular sub-kernel. The Kuwahara filter calculates the mean misorientation and variance for each sub-kernel and replaces the centred pixel with the average orientation having the lowest variance. The average process aborts if the misorientation of a pixel within the sub-kernel with the lowest variance is higher than a certain value, which is set to 2° . This prevents errors close to grain boundaries.

4.7.4 Subgrain characterization

Subgrain boundaries are detected by using misorientation measurements. GNBs arise if two cell-blocks with different orientations converge; consequently, the spacing between two misorientation peaks determines the subgrain size. For calculating this parameter, as well as the mean misorientation of GNBs, at least ten line scans are utilized. Figure 27 displays a typical line scan, where the subgrain size can be easily determined by measuring the distance between the misorientation peaks higher than 4° .

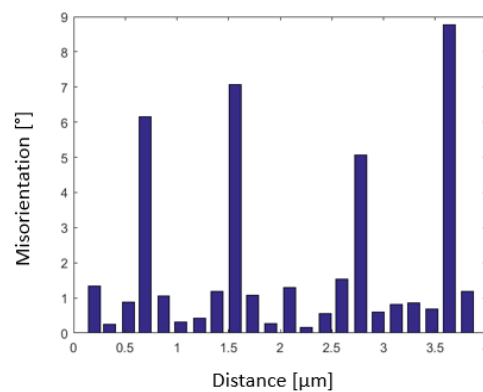


Figure 27: Misorientation measurement perpendicular to cell bands; peaks higher 4° characterize GNBs

5 Results

This section presents the heat treatment simulation via MatCalc as well as the results of hardness tests and EBSD investigations. Discussions of the obtained data are provided in chapter 6.

5.1 Simulation

The following MatCalc simulation Figure 28 rebuilds the heat treatment and calculates the phase fraction of GP-zones, β' and β'' precipitates. An intended solid solution state without precipitates is formed during the solid solution heat treatment at a temperature of 540 °C while GP-zones, as well as β'' precipitates are generated during natural aging. However, they immediately dissolve during the artificial heating process at 350 °C, where stable β' precipitates are formed. Hence, the MatCalc simulation in Figure 28 excludes the influence of precipitation hardening during further annealing processes at a temperature of 325 °C, and work hardening is the only relevant strengthening mechanism.

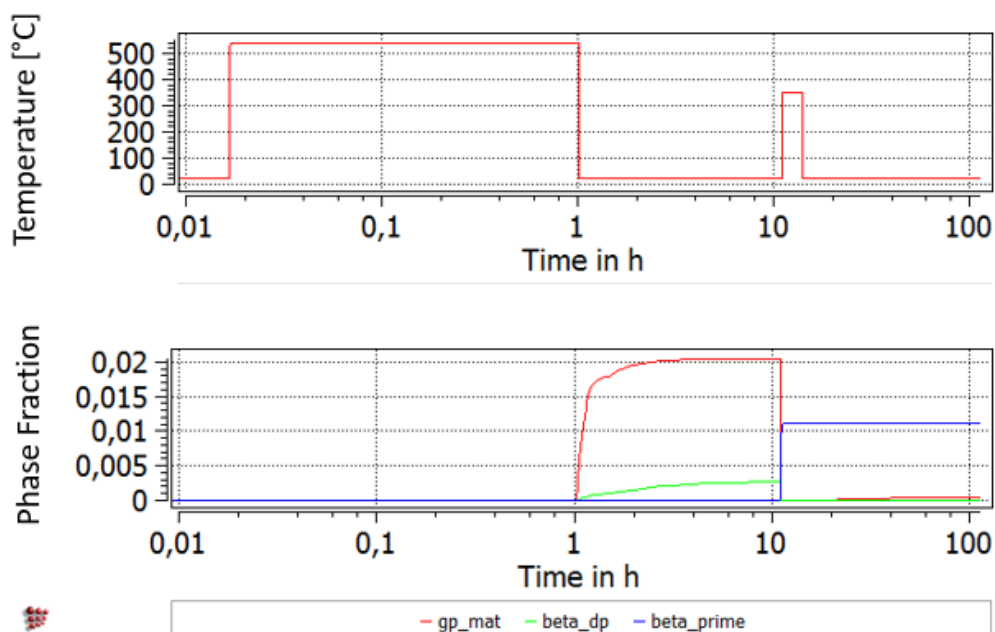


Figure 28: MatCalc simulation of the phase fraction of GP-zones, β'' and β' precipitates for the adjusted heat treatment

5.2 Hardness tests

The softening behaviour, based on the isothermal annealing process, is illustrated in Figure 29 for both deformation states of (a) $\varphi = 0.4$ and (b) $\varphi = 0.7$. Seven Brinell hardness tests are performed for each annealing time along the specimen's centreline, specifying an uneven compression over the cross section of the workpiece. Each experiment is conducted twice, leading to mean hardness values of each position.

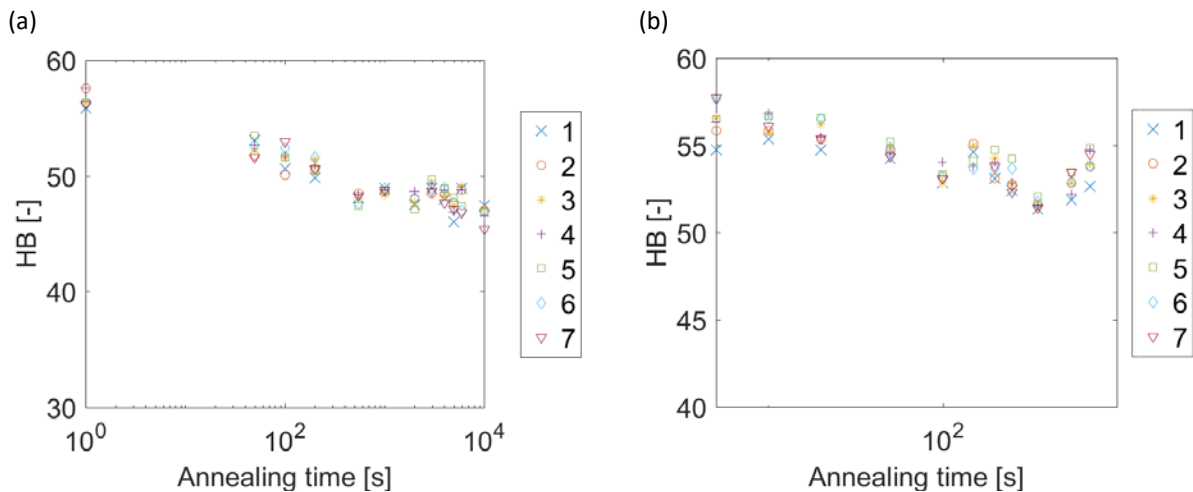


Figure 29: Brinell hardness values as function of the annealing time for both deformation states of (a) $\varphi = 0.4$ and (b) $\varphi = 0.7$. For each annealing time, seven tests are performed on different positions along the specimen's centreline

As expected, hardness decreases with increasing annealing time. Varying hardness values within one specimen reflect uneven deformation states. The maximum deviation within one specimen yields 9.3% and was obtained by a specimen deformed to a final strain of $\varphi = 0.4$, without further annealing process. Since low hardness values are often detected at position 1 and/or position 7, which are situated on the edge of the specimen, a connection to the deformation cross, as described in 3.4, can be established.

The displayed curves in Figure 30 correspond to the hardness values of the centre points (position 4 in Figure 29) for the deformation states $\varphi = 0.4$ and $\varphi = 0.7$. Each experiment is conducted twice, leading to mean hardness values. An increase of strain involves an increase of hardness but the shape of both curves during annealing are similar and seem to be independent of the deformation state. The discontinuous drop can be explained by inhomogeneous deformations or measuring inaccuracy.

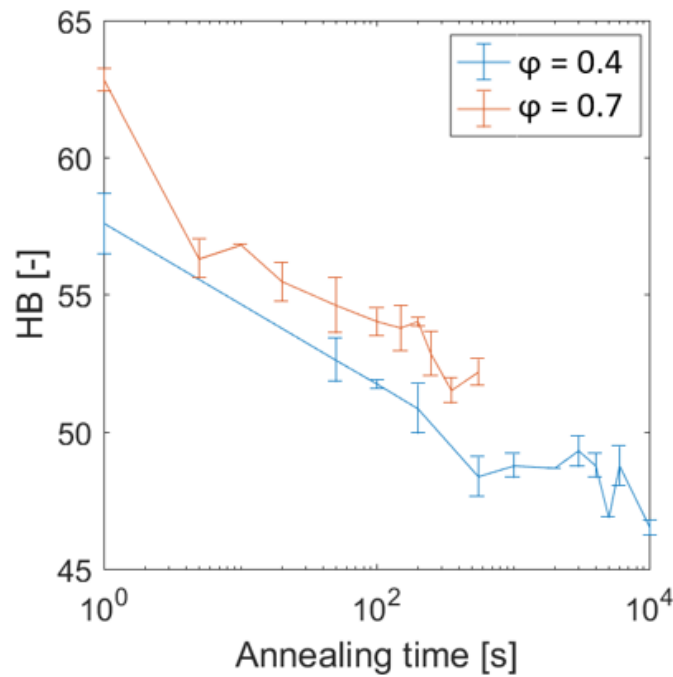


Figure 30: Softening behaviour of both deformation states ($\varphi = 0.4$ and $\varphi = 0.7$)

5.3 EBSD investigations

This chapter presents the results of EBSD investigations, including the characterization of the microstructures. Three EBSD observations of different heat treatments are made on each deformation state to point out the influence of the annealing process on the arrangement of the dislocations. An area of $66 \mu\text{m} \times 120 \mu\text{m}$ is scanned and an orientation map is generated automatically (see section 3.3.2). Each colour defines a specific orientation, which is shown in the inverse pole figure next to the EBSD maps. Typical cell-band structures, as described in 3.1, are detected, but statistically trapped dislocations within the substructure prevent assignments to IDBs of low misorientation. Kernel Average Misorientation (KAM) maps illustrate the existence of cells, and are shown in the Appendix for all investigated specimens. In case of detecting sets of cell-bands, the average angle between the dominant directions and the rolling direction of at least three band structures are calculated. The term rolling direction is used in reference to literature, but concerning compression tests, it characterizes the direction perpendicular to the applied stresses.

5.3.1 Deformation state: $\phi = 0.7$; annealing time: none

Figure 31a shows the microstructure after a deformation to a strain of 0.7 without subsequent annealing processes. The grains are elongated toward the rolling direction, and the grain in the middle of Figure 31a is approximately 41 μm thick. Within the grain, the orientation is not homogenous, represented by a variation of the colours. With higher magnification, as shown in Figure 31b, cell bands are classified. Black areas are non-indexed pixels, which can be traced on defects such as pores or on overlapping Kikuchi patterns, where no specific orientation fits. Consequently, non-indexed pixels agglomerate at grain boundaries or high deformed positions. The evenly distributed, single-coloured regions of a few pixels can be explained by precipitates, but are not further considered in this analysis.

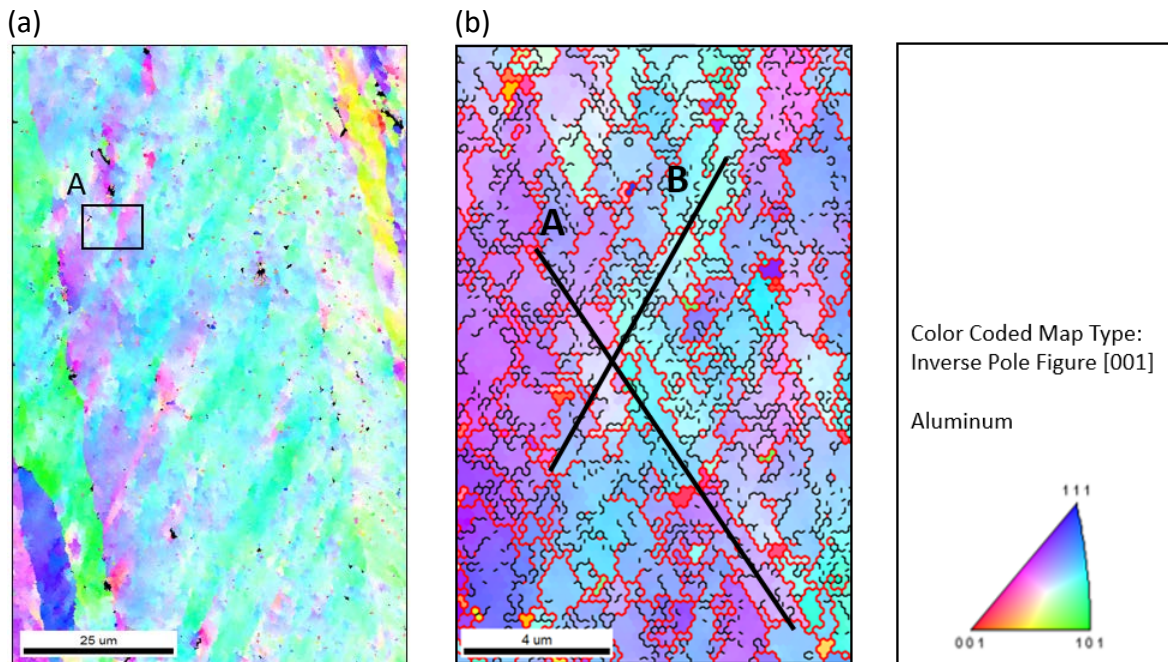


Figure 31: Deformation to a final strain of $\phi = 0.7$, without subsequent annealing process; (b) is an enlargement of the rectangle A in (a) including GNBs with misorientations higher 4°, marked as red lines

Figure 31b shows the enlargement of detail A in (a) whereas black lines indicate misorientations between 1.5° and 4° and red lines show misorientations higher than 4°. Those values are chosen to differentiate between the delineation of GNBs and IDBs. Though no symmetric band structure extends over the whole grain, a local tendency can be detected. The black lines A and B in Figure 31b demonstrate the directions of two intersecting sets of cell-bands. Both sets arise during deformation by the activation of different slip systems, which is a common feature of deformed aluminium alloys [17]. The angle between a parallel

set of cell-bands and the rolling direction is 38° , which is in accordance to previous observations [24,25,26]. The width of a cell-band is obtained by plotting the misorientation along a line scan and subsequently by measuring the spacing between those peaks that are related to GNBs. One example for obtained misorientation along a line scan is provided in Figure 32a and a histogram of all obtained spacings of GNBs is shown in Figure 32b.

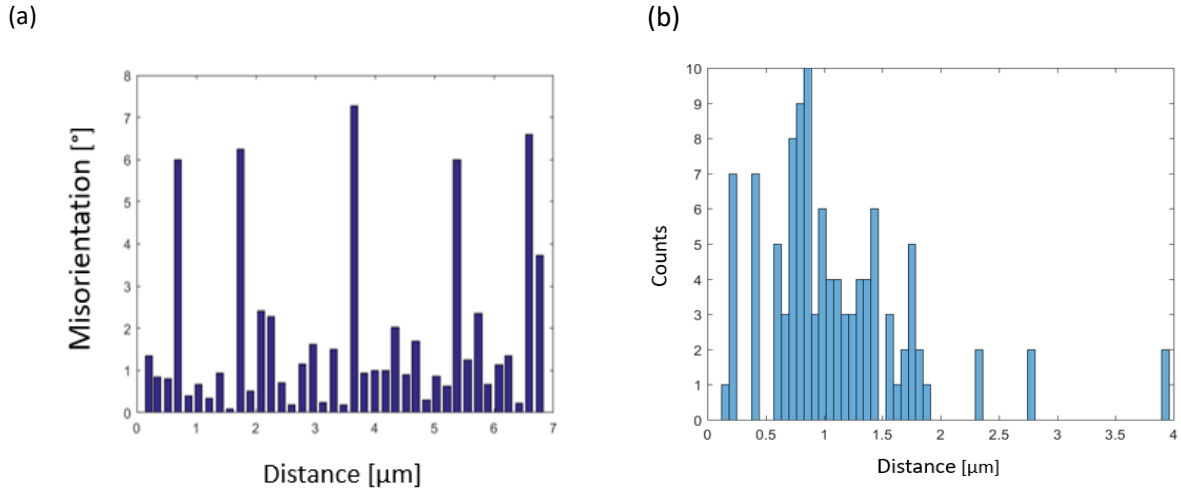


Figure 32: (a) Misorientation measurement perpendicular to cell bands; peaks higher 4° characterize GNBs; (b) histogram of the spacings of GNBs

While GNBs can be allocated precisely, dislocations seem to arrange statistically within the cell-band, and no identification of individual cells is possible in the obtained orientation maps. However, according to the similitude principle, which relates the density of dislocations to the average length of a virtual uniform dislocation microstructure [27], the spacing between GNBs is sufficient. The average spacing between GNBs, as well as the misorientations of GNBs, are calculated by using ten line scans at different positions. The mean misorientation angle of cell-band boundaries is 8.24° , and the spacing yields $1.04 \mu\text{m}$.

5.3.2 Deformation state: $\varphi = 0.7$; annealing time: 150 sec

Figure 33 shows the microstructure after a deformation to a true strain of 0.7 and subsequent annealing for 150 seconds at a temperature of 325°C . Again, a substructure is detected within the grain, having a predominant direction that is manifested in an angle of approximately 30° to the rolling direction. Though the colour differs strongly within the grain, measured low misorientations exclude features like high angle boundaries (misorientation $> 15^\circ$), as it might appear in high deformed specimens.

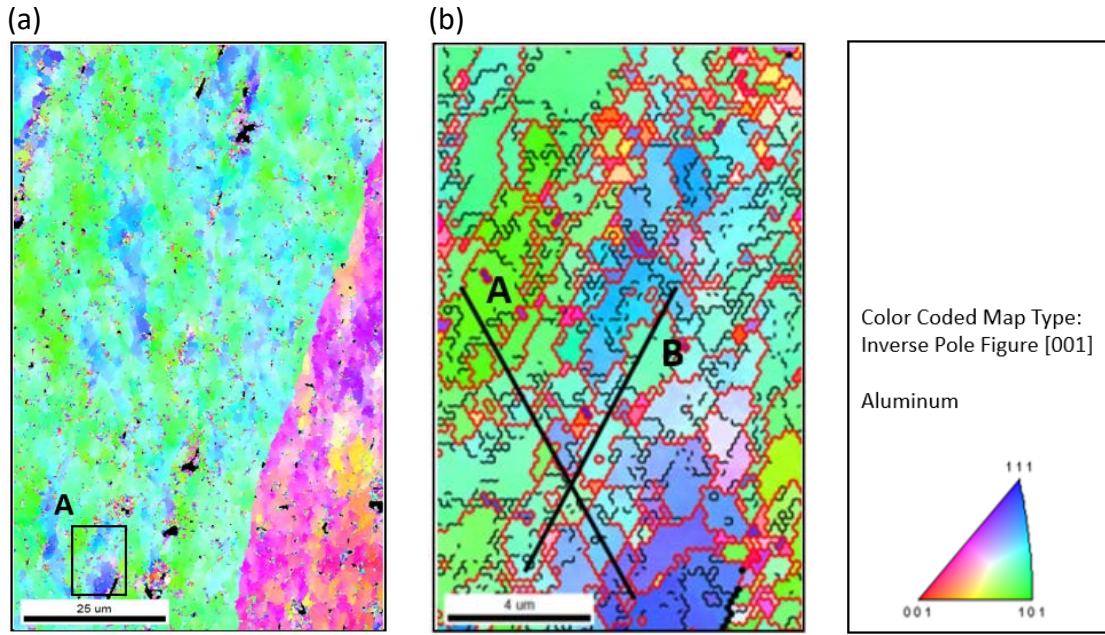


Figure 33: (a) Microstructure after a deformation to a final true strain $\phi = 0.7$ with subsequent annealing for 150 seconds at 325 °C; (b) enlargement of rectangle A in (a), red lines indicate GNBs

The enlargement of detail A shows two intersecting sets of cell bands. The red boundaries indicate GNBs, and black lines symbolize misorientations between 1.5° and 4°. The black lines A and B indicate the predominant directions of the cell-bands. Line scans perpendicular to cell-bands result in misorientation plots as a function of length, as given in Figure 34a. The impossibility to assign individual cells in the microstructure might result on the spectrum of noise of the images, which is tried to be reduced by the Kuwahara filter (4.7.3). Figure 34b displays a histogram of the spacings of GNBs.

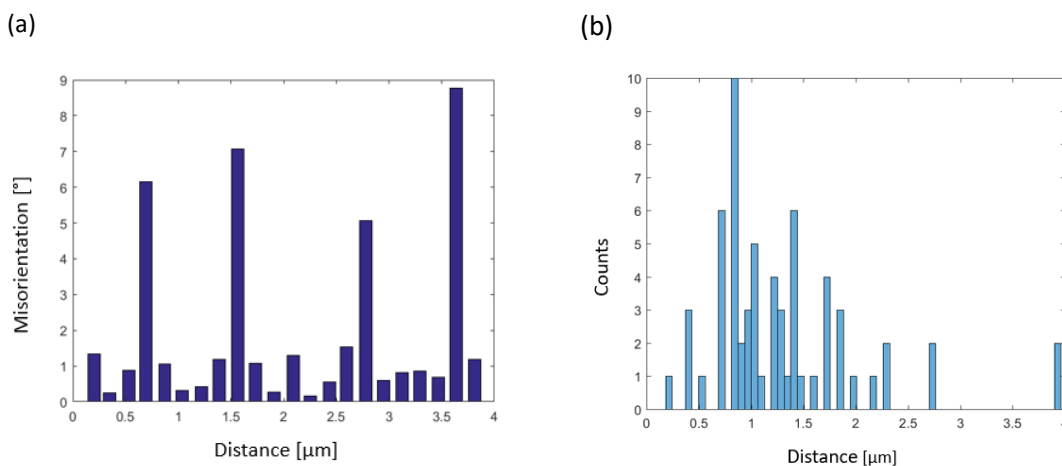


Figure 34: (a) Misorientation measurement perpendicular to cell bands; peaks higher 4° characterize GNBs; (b) histogram of the spacings of GNBs

The mean boundary misorientation, evaluated by ten line scans, is 8.58°, and the spacing

between GNBs is $1.16\ \mu\text{m}$.

5.3.3 Deformation state: $\varphi = 0.7$; annealing time: 700 sec

The microstructure of the deformed specimens to a true strain of 0.7 and subsequent annealing for 700 seconds at $325\ ^\circ\text{C}$, is shown in Figure 35. On this scale, no dominant cell-band structure can be detected; but regarding colour changes within each grain, subgrains can be adumbrated, and are shown at a higher magnification in Figure 35b,c. The black lines indicate grain boundaries; subgrains are restricted by red lines, defining a misorientation angle of more than 4° . By annealing processes and resulting static recovery, the microstructure changes by coarsening of the subgrains. Detail A and detail B in Figure 35a display two advanced subgrain coarsening levels. In contrast to detail A, cell band structures can be detected in detail B. The dominant directions are displayed by two black lines in Figure 35c. Misorientation measurements by the linear intersection method yields a mean orientation change due to GNBs of 8.91° and a mean spacing of $1.56\ \mu\text{m}$.

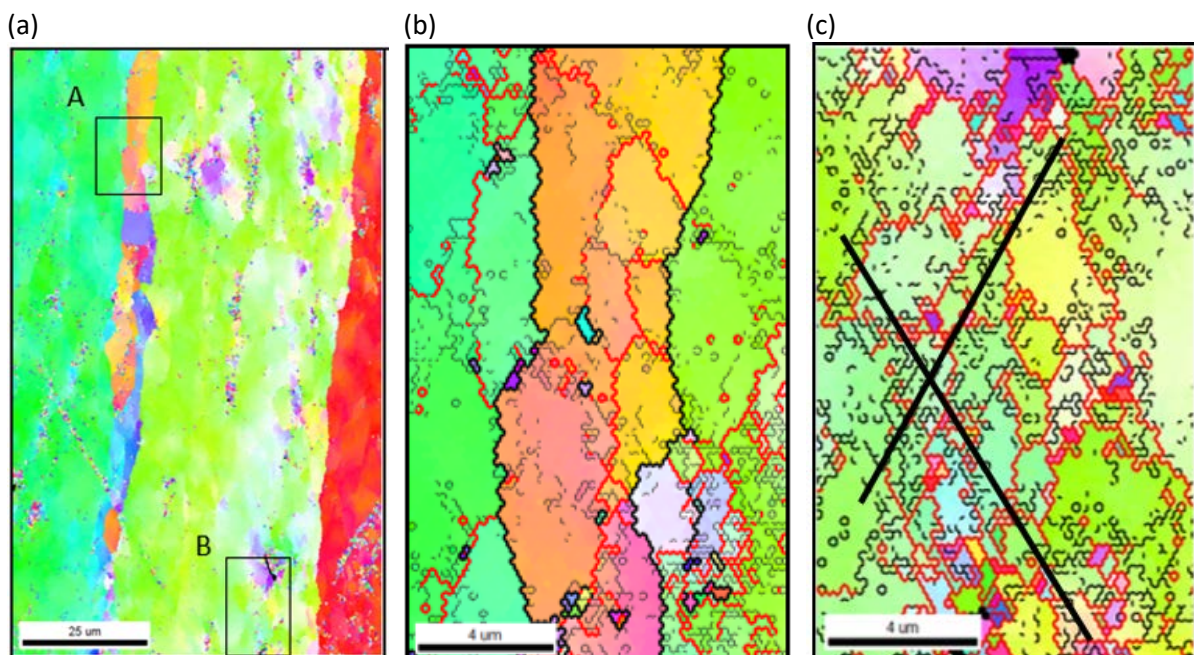


Figure 35: (a) Microstructure after a deformation to a final true strain $\varphi = 0.7$ with subsequent annealing for 700 seconds at $325\ ^\circ\text{C}$; (b) and (c) show enlargements of both rectangles A and B, red lines indicate GNBs

The following histogram in Figure 36a displays the distribution of all measured substructure spacings. Distances between $1.05\ \mu\text{m}$ and $1.14\ \mu\text{m}$ are detected most often and are related to areas in detail B, whereas higher boundary spacings are related to subgrains as displayed in detail A. Figure 36b shows a typical line scan to obtain misorientation angles.

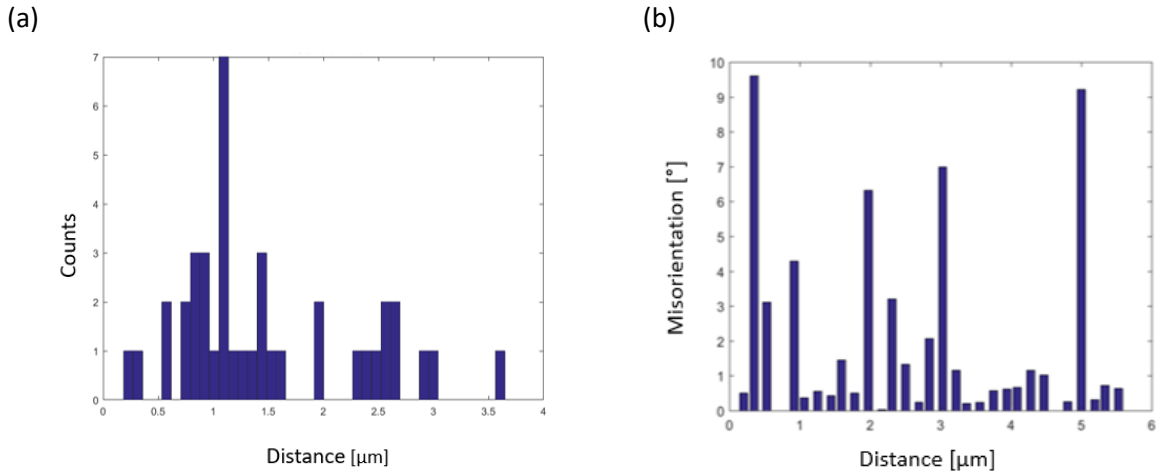


Figure 36: (a) Histogram of the spacings of GNBs after annealing for 700 seconds; (b) misorientation measurement after a deformation to a final strain of $\phi = 0.7$ and subsequent annealing for 700 seconds at 325 °C

5.3.4 Deformation state: $\phi = 0.4$; annealing time: none

The following orientation maps are obtained by EBSD investigations of specimen that are deformed to a true strain of 0.4. Figure 37 shows the microstructure after a compression at room temperature. Within the aligned elongated grains, orientation changes occur due to subgrain boundaries, which are shown at higher magnifications in Figure 37b.

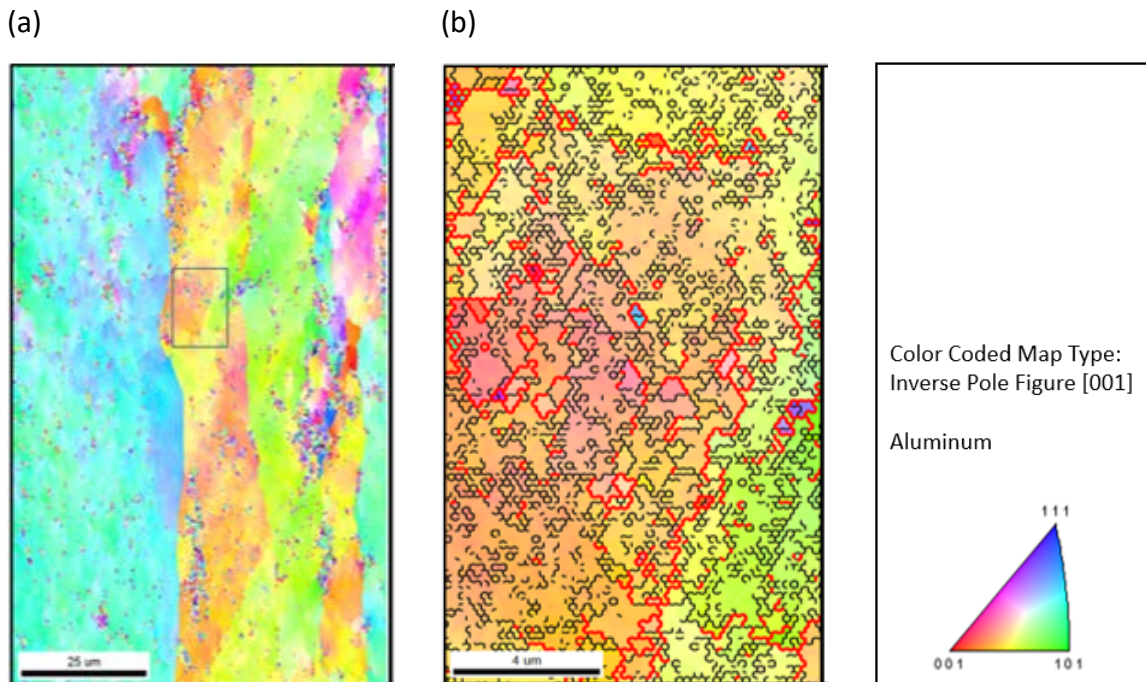


Figure 37: Deformation to a final strain of $\phi = 0.4$, without subsequent annealing process; (b) is an enlargement of the rectangle in (a), including GNBs with misorientations higher 4°, marked as red lines

The evolution of cell-bands are less sophisticated compared to the obtained microstructure after a compression to a true strain of 0.7, as shown in Figure 37b. However, GNBs can also be allocated and the mean misorientation angle, as well as the spacings can be measured, as displayed in Figure 38a. The mean boundary misorientation, evaluated by ten line scans, is 6.83° , and the spacing between GNBs is $1.46 \mu\text{m}$. Figure 38b shows a histogram of the spacings of GNBs.

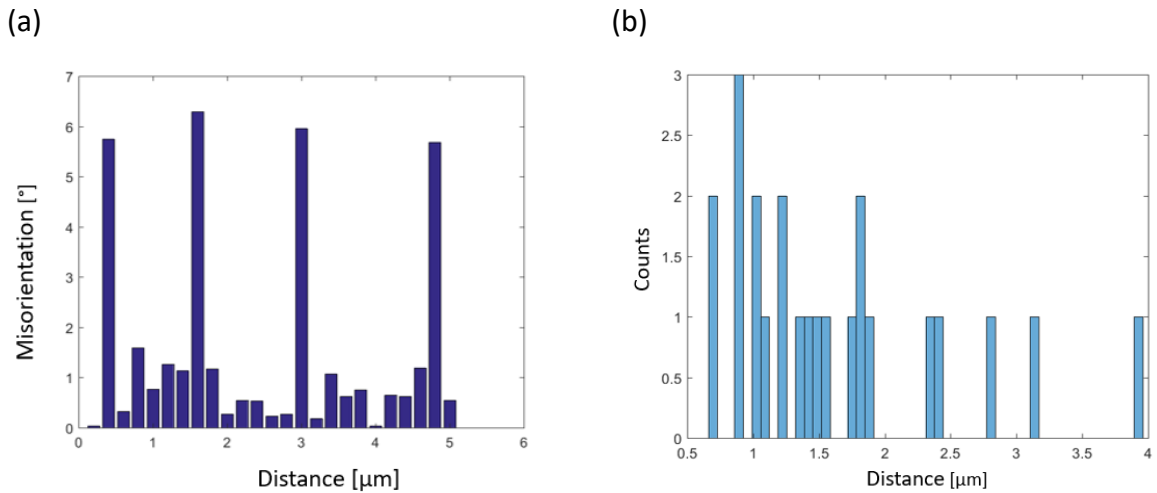


Figure 38: (a) Misorientation measurement; (b) histogram of the spacings of GNBs

5.3.5 Deformation state: $\varphi = 0.4$; annealing time: 3.000 sec

After a heat treatment for 3.000 seconds at 325°C , a microstructure, as shown in Figure 39a, is obtained by EBSD investigations. Cell-band structures are not visible, but subgrains of a few micrometres arise.

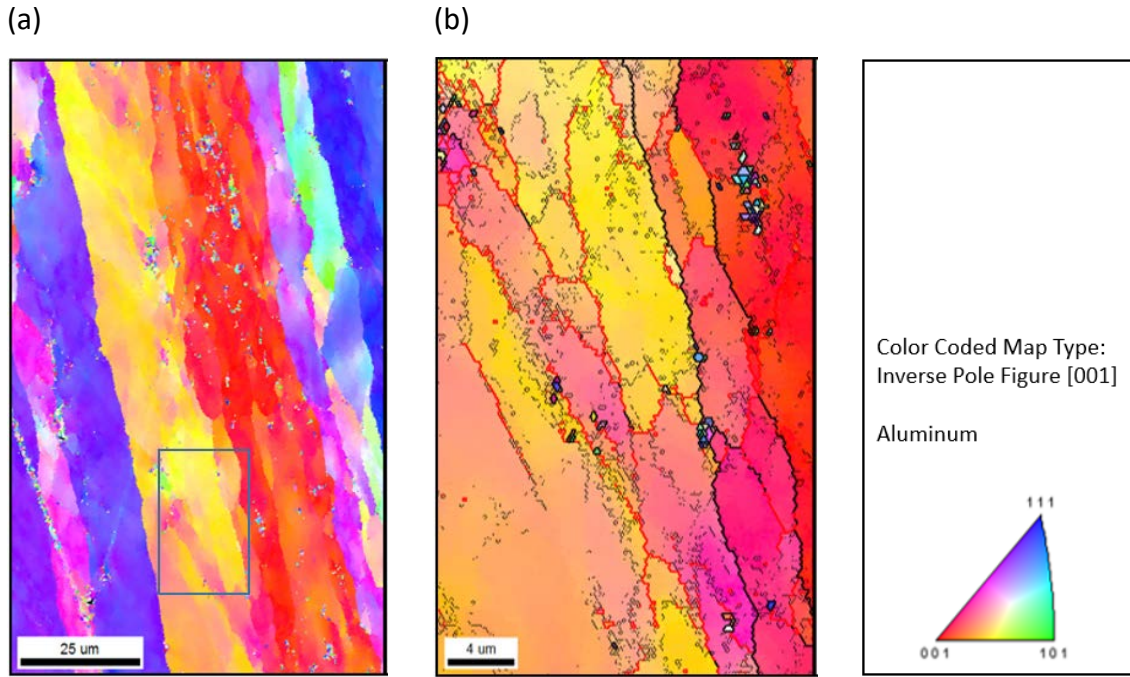


Figure 39: Deformation to a final strain of $\phi = 0.4$, with subsequent annealing for 700 seconds at 325 °C (b) is an enlargement of the rectangle A in (a) including GNBs with misorientations higher 4°, marked as red lines

Thick black lines symbolize grain boundaries, and red lines delineate misorientation higher than 4°. Within the subgrains, no cell structure is perceived regarding misorientation measurements, as shown in Figure 39b, but the formation of interior cells is not further considered in the similitude principle. Misorientation peaks higher than 4° define GNBs and exhibit a mean misorientation angle of 8.07°. The mean subgrain size with 2.44 μm depicts a coarsening process due to static recovery, which is reflected in the histogram in Figure 40b.

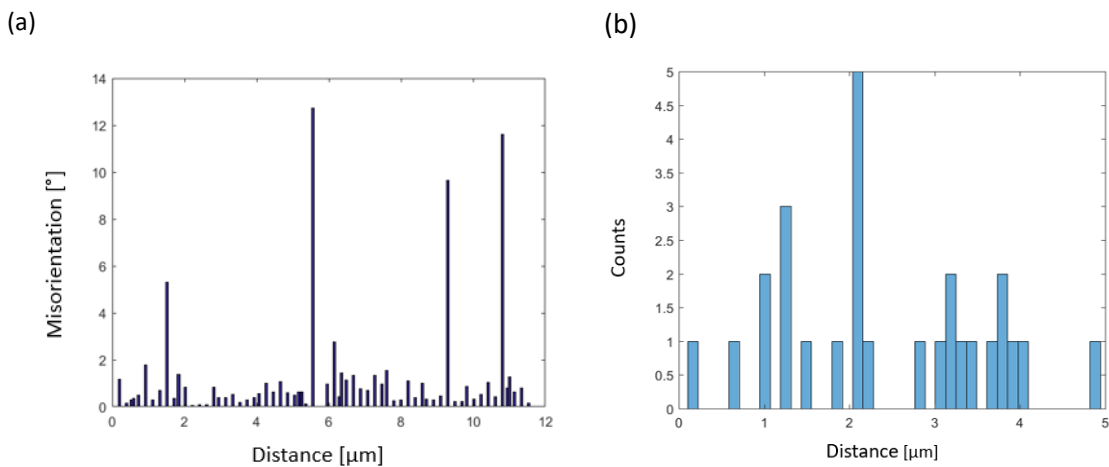


Figure 40: (a) Misorientation measurement after a deformation to a final strain of $\phi = 0.4$ and subsequent annealing for 3.000 seconds at 325 °C; (b) histogram of the spacings of GNBs after annealing for 700 seconds

5.3.6 Deformation state: $\phi = 0.4$; annealing time: 10.000 sec

After an annealing time of 10.000 seconds, recrystallized grains are visible in Figure 41a. They are identified by one homogenous colour, deduced from dislocation-free zones. Beside recrystallized areas, recovered cell structures still exist as shown in Figure 41b.

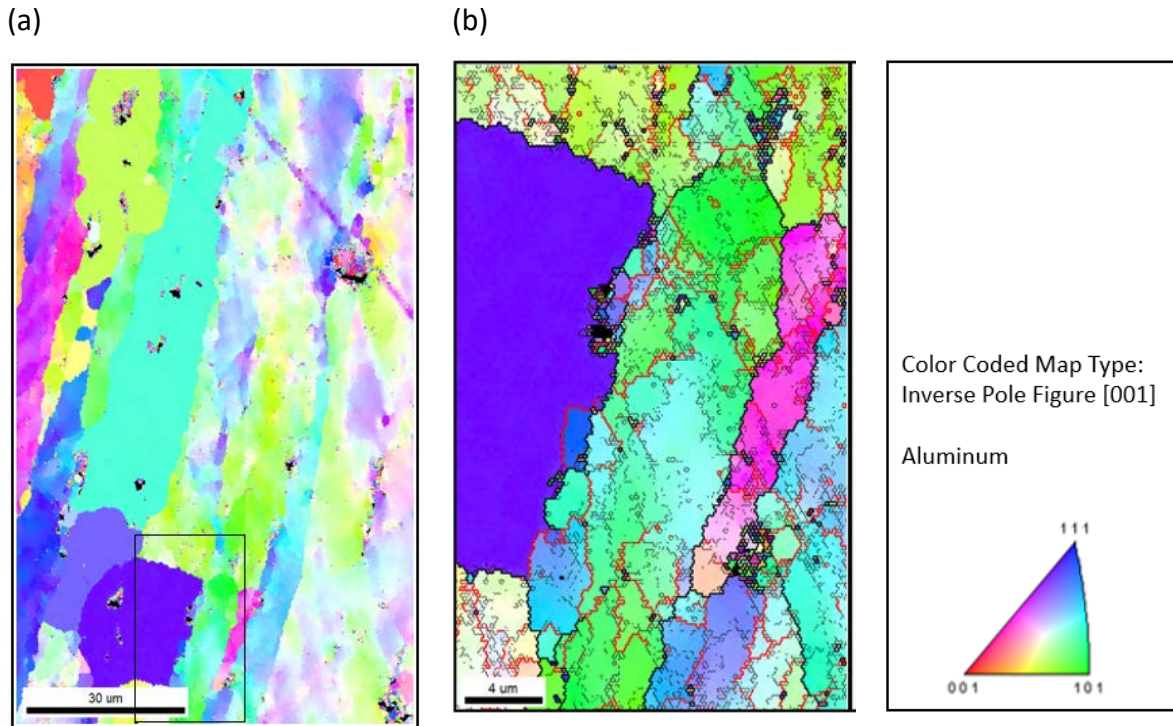


Figure 41: Deformation to a final strain of $\phi = 0.4$, with subsequent annealing for 10.000 seconds at 325 °C; (b) is an enlargement of the rectangle in (a) including GNBs with misorientations higher 4°, marked as red lines

Since the extended Kocks-Mecking approach considers dynamic and static recovery, the following characterization of the substructure focuses on received subgrains. Thick, black lines in Figure 41b indicate grain boundaries, while subgrains are delineated by red lines that mark misorientations higher than 4°. A Kernel Average Misorientation (KAM) map (see Appendix) highlights microstructural aspects of recovered and recrystallized areas and is consulted for finding appropriate areas for misorientation measurements. The mean misorientation of the subgrain-boundaries results in 8.86°, and an average subgrain size yields 3.08 μm . One particular subgrain is identified by each line scan, as shown exemplary in Figure 42a. A histogram of the distances between GNBs in Figure 42b indicates the existence of large subgrains, which develop during static recovery.

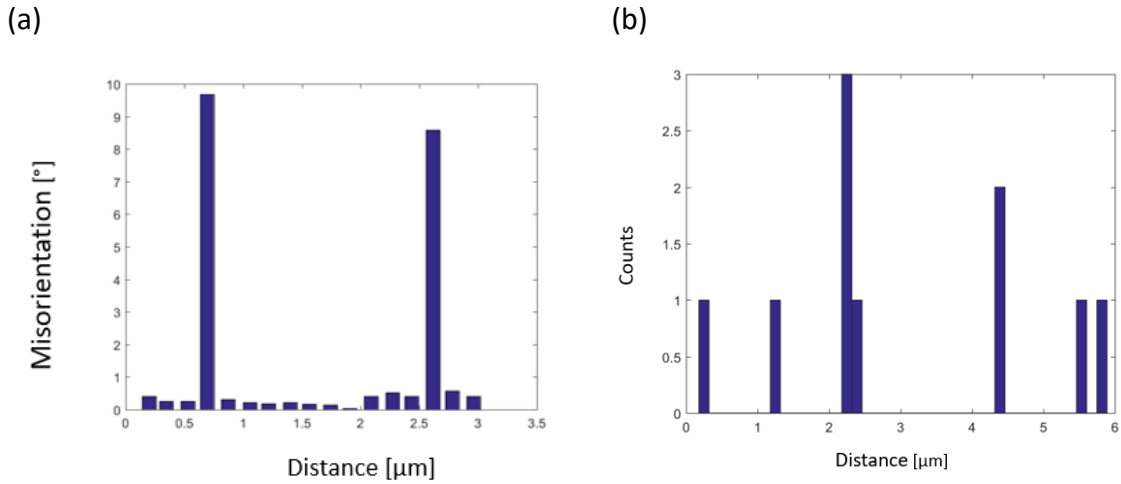


Figure 42: (a) Misorientation measurement after a deformation to a final strain of $\varphi = 0.4$ and subsequent annealing for 10.000 seconds at 325 °C; (b) histogram of the spacings of GNBs

5.3.7 Compilation of experimental results

The evolution of the subgrain sizes, misorientation angles and lengths of GNBs during static recovery are displayed in the following four plots (Figure 43a,b; Figure 44a,b). Figure 43 illustrates that higher strains cause higher mean misorientations by the arising dislocation density and lower the mean subgrain sizes, as described in 3.3.3. These relations are in good agreement with experimental results in literature [12, 14, 16]. With increasing annealing time, both, the subgrain size and the misorientation increases.

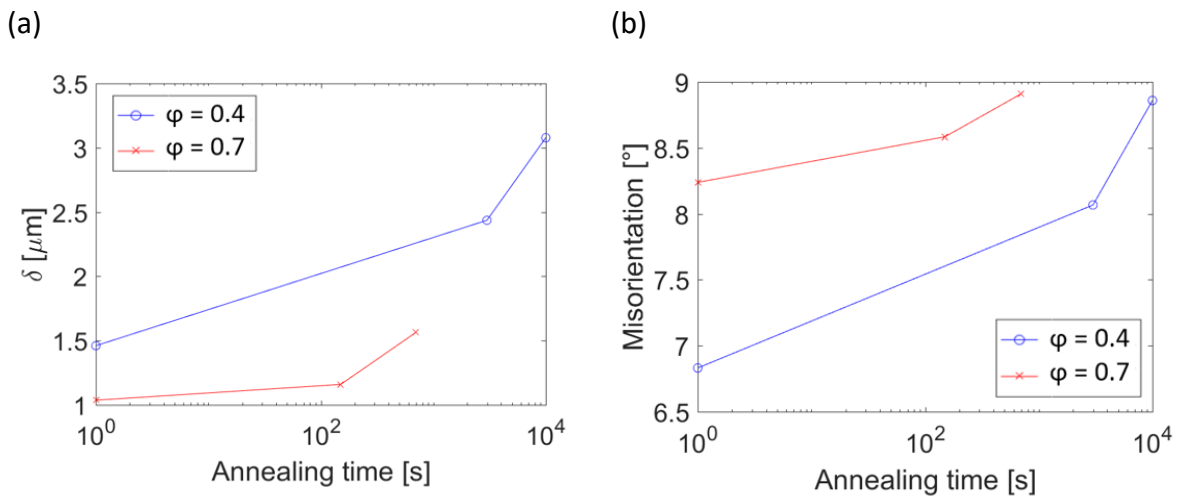


Figure 43: Misorientation (a) and subgrain size (b) as a function of the annealing-time at 325°C; considering two deformation states: $\varphi = 0.4$ and $\varphi = 0.7$

Figure 44a depicts an almost linear relation between the misorientation angle of GNBs and the subgrain size. The decrease of the total length of GNBs within an area of 66 μm x 120 μm, which is higher for more deformed specimens, is displayed in Figure 44b.

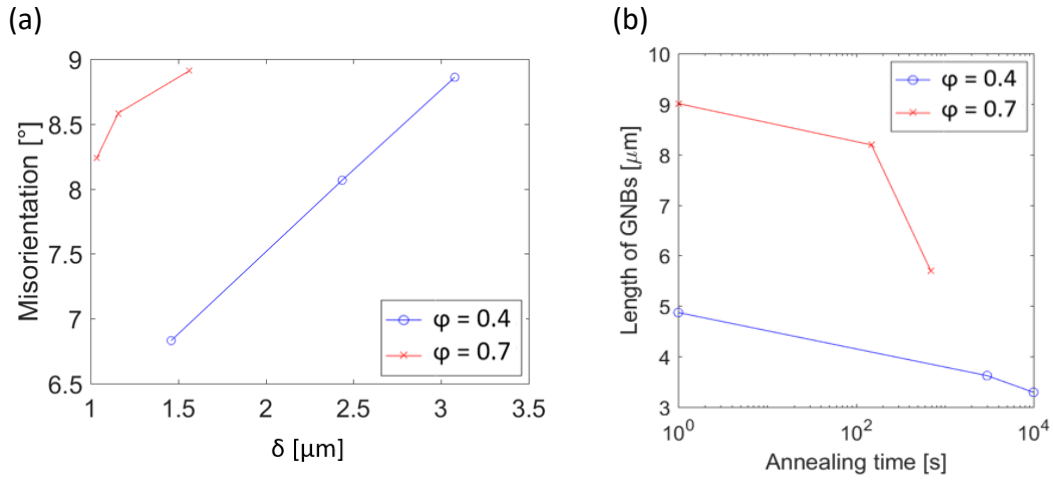


Figure 44: Misorientation as a function of the grain size (a); length of GNBs as a function of annealing time for the deformation states $\phi = 0.4$ and $\phi = 0.7$ (b)

Following tables show all results obtained by EBSD investigations at a glance.

Table 5: Subgrain characterization of the deformation state of $\phi = 0.4$

Annealing time [sec]	0	3.000	10.000
Misorientation [°]	6.83	8.07	8.86
Subgrain size [μm]	1.46	2.44	3.08
Length of GNBs [μm]	4.87	3.62	3.29

Table 6: Subgrain characterization of the deformation state of $\phi = 0.7$

Annealing time [sec]	0	150	700
Misorientation [°]	8.24	8.58	8.91
Subgrain size [μm]	1.04	1.16	1.56
Length of GNBs [μm]	9.01	8.19	5.69

6 Discussion

Hardness tests are performed to describe the softening behaviour due to recovery processes. Figure 45a shows the obtained hardness values in terms of the annealing time at 325 °C for both final deformation states ($\varphi = 0.4$ and $\varphi = 0.7$). Figure 45b illustrates isothermal annealing at a range of temperatures for cold rolled Al0.43 wt% Fe0.09 wt% Si alloys and is taken from literature.

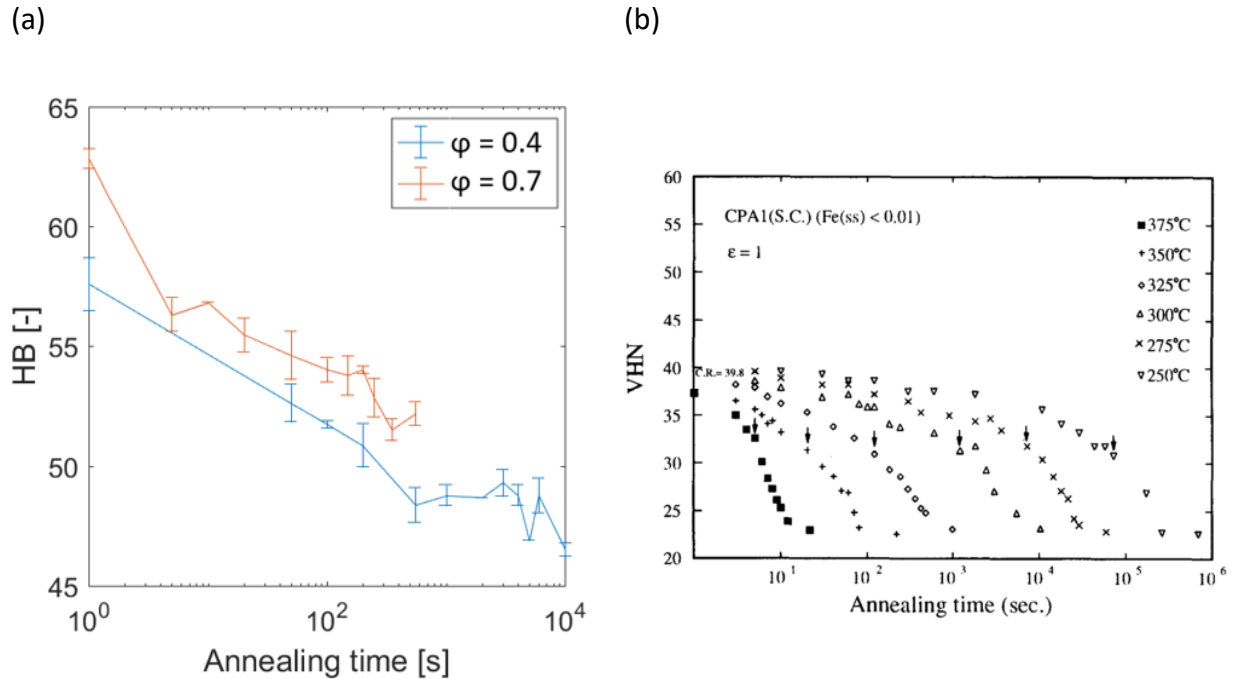










Figure 45: (a) Hardness values as a function of annealing time: experimental results at an annealing temperature of 325 °C; (b) cold rolled ($\epsilon = 1$) Al0.43 wt% Fe0.09 wt% Si alloys for a range of annealing temperatures

As expected, an increasing annealing temperature shifts the value of strength to shorter annealing times. The black arrows represent a recrystallization of about 10%, which is ascertained by microstructural investigations. The recrystallization process seems to start at almost the same hardness values for all temperatures, followed by an increase of the slope of the curves by exceeding a recrystallized fraction of 10%. Since a deformation state of $\epsilon = 1$ corresponds to a final true strain of $\varphi = 0.7$, a comparison between the obtained experimental results in Figure 45a and the results at 325 °C from literature is possible. Though the content of the alloys varies, the shape of the curves is similar and a specific softening behaviour is determined. As shown in Figure 45a, an increase of strain involves an increase in hardness. An almost linear decrease of the obtained Brinell values in the semi-logarithmic plot, as well as

microstructural investigations justify the assumption of static recovery during the annealing processes. The fraction of recrystallization can be determined by evaluating EBSD maps with OIM. Therefore, per definition, recrystallization occurs, if the average grain orientation spread, which calculates the average misorientation between all data points within a grain, stays below 1.5° . Except for the annealing time of 10.000 seconds, recrystallization is negligible. Since hardness values can be converted to stress values, dislocation densities can be calculated by the Taylor equation Eq. (11). However, these values differ widely from both, the predicted values by the Kocks-Mecking model, and the experimentally obtained dislocation densities. Consequently, hardness tests reflect the progress of recovery properly, but no correlation to state parameters, such as the dislocation density, can be established. The experimental results indicate, that the evolution of the microstructure can be described by the spacing of GNBs, which continuously increases during static recovery. With the similitude principle, dislocation densities are determined, which can be compared to predicted values of the Kocks-Mecking model. The calibration of the A, B and C parameters are discussed, using obtained flow curves for the A and B parameter, as well as the obtained evolution of the dislocation densities for the C parameter. For calibrating the C parameter of the Kocks-Mecking model, microstructural observations are used. The EBSD images in 5.3 show typical cell-band structures, including GNBs. Observations by Q. Liu and N. Hansen [18] indicate a decrease of the distance between GNBs as well as an increase of the misorientation of adjacent cell-bands with increasing strain. This is in good agreement with the obtained results listed in Table 7.

Table 7: Influence of increasing deformation and annealing time on misorientation, subgrain size and the length of GNBs

		Misorientation	Subgrain size	Length of GNBs
Strain				
Annealing time				

With continuing annealing time, both, the mean misorientation as well as the mean subgrain size increase. This is in good agreement with Furu and Nes [23], who explain this correlation with the existence of orientation gradients. Long-range gradients are expected to remain

approximately constant during annealing, leading to increasing misorientation per subgrain due to subgrain growth [39]. Though the Read-Schockley Eq. (6) predicts an increasing subboundary energy, the total stored energy is minimized due to a reduction of the length of GNBs. With the combination of the measured GNBs distances and the application of the similitude principle Eq. (12), the evolution of the dislocation density during static recovery can be calculated. With the C-term in the extended Kocks-Mecking approach in Eq. (18), the thermally activated reduction of the dislocation density is calculated and shown as solid lines in Figure 46. The starting points of $1.06 \times 10^{14} [1/m^2]$ for a deformation to a true strain of $\varphi = 0.4$, and $2.10 \times 10^{14} [1/m^2]$ for a final true strain of $\varphi = 0.7$, are calculated by the obtained subgrain sizes, which result from deformed specimens without subsequent annealing processes. After 10.000 seconds, a measured subgrain size of $3.08 \mu m$ corresponds to a dislocation density of $2.38 \times 10^{13} [1/m^2]$, which is a legitimate assumption for the equilibrium dislocation density (ρ_{equ}) caused by recovery. The fitting parameter C is set to 6×10^{-4} . This is justified by a good accordance of modelled and measured curves as shown in Figure 46.

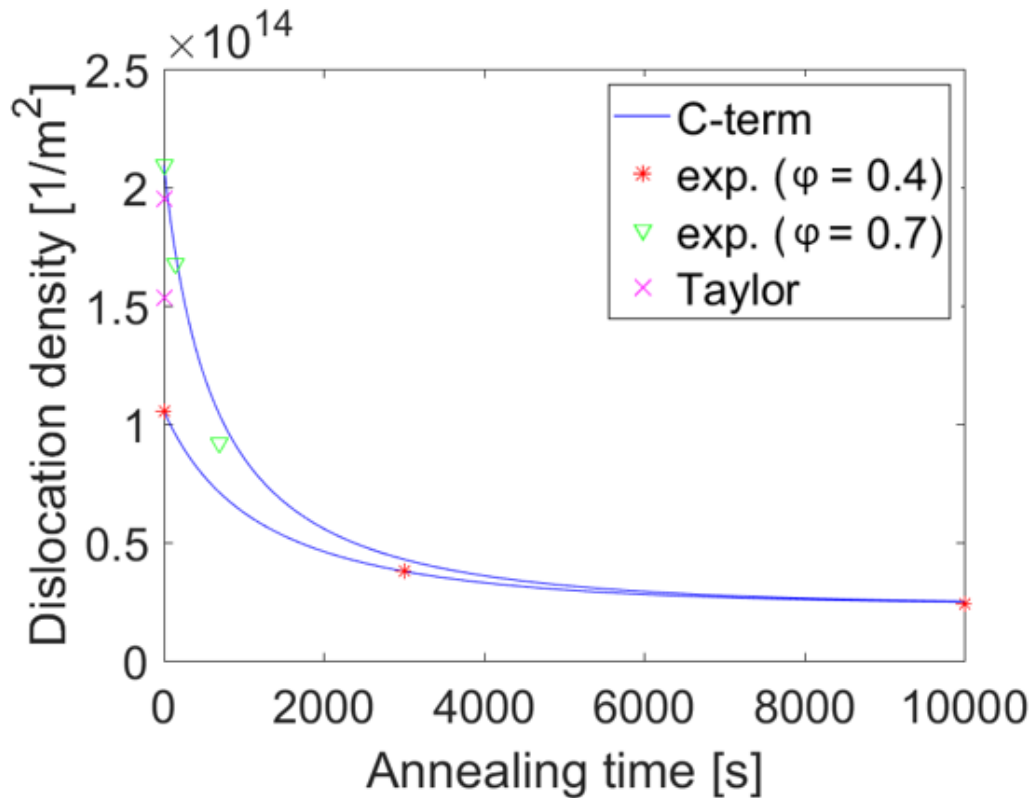


Figure 46: Dislocation density (ρ) as a function of annealing time (t) at $325^\circ C$; solid lines are modelled by the extended Kocks-Mecking approach; stars and triangles ($\varphi = 0.4$ and $\varphi = 0.7$) are calculated by experimental values and the similitude principle; crosses are calculated with the Taylor relation

The shape of both solid lines is identical but shifted due to different initial dislocation densities. Another possibility to calculate the initial dislocation density is to plug in the final stress-value of the flow curves at $\varphi = 0.4$ and $\varphi = 0.7$ into the Taylor equation, Eq. (11). The stress values are reduced by the yield strength to describe the strengthening behaviour of stage III. Both obtained dislocation values for $\varphi = 0.4$ and $\varphi = 0.7$ are plotted as magenta crosses in Figure 46. The magnitude of these values fit to dislocation densities that are obtained by the experiments, but predict a much lower generation of dislocations between both deformation states.

While the C parameter is calibrated by microstructural observations, the parameters A and B are determined as described in section 3.7. Two representative flow curves for both deformation states ($\varphi = 0.4$ and $\varphi = 0.7$) are plotted in Figure 47a, while the slope (θ) of the stress-strain curve is shown as a function of stress in the Kocks-plot in Figure 47b.

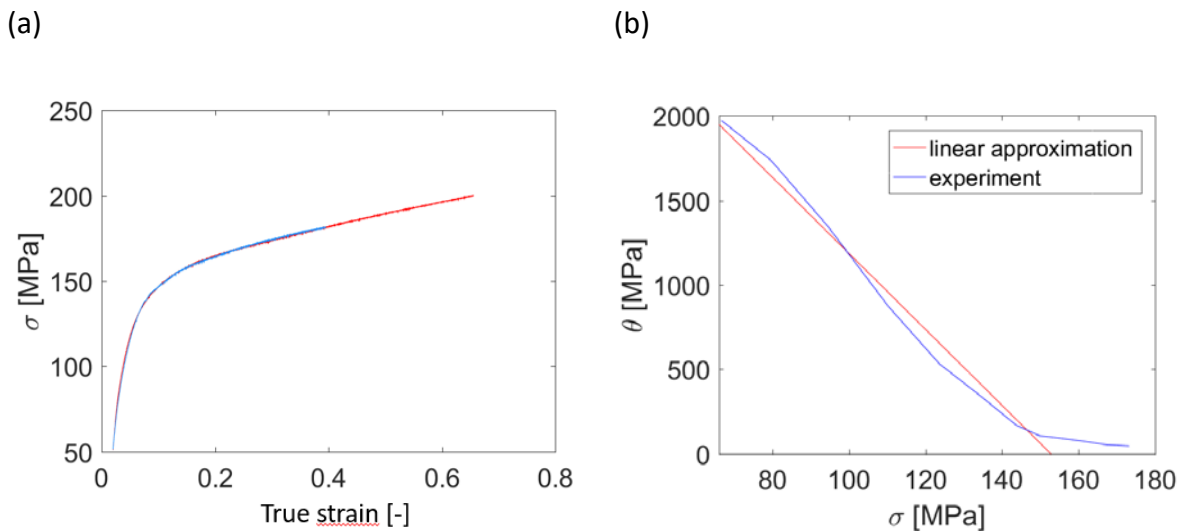


Figure 47: (a) Flow curves to final strains of $\varphi = 0.4$ and $\varphi = 0.7$; (b) Kocks-plot: blue: slope (θ) of the stress-strain curve as a function of σ [MPa], red: linear approximation of stage III

Stage III is characterized by a linear decrease of θ , which is approximated by the red line in Figure 47b. An almost constant slope of the flow curve defines stage IV. The intersection point with the x-axis determines the saturation stress σ_∞ , and the initial slope defines θ_0 . With these two characteristic parameters, A and B in Eq. (17) and Eq. (18) are calculated as described in section 3.7: $A = 23.15$ and $B = 7.33$. The blue curve in Figure 48 indicates the experimentally determined flow curve, whereas the red one indicates the calculated curve by the Kocks-Mecking approach. Due to the fact that the Kocks-Mecking approach cannot describe the constant slope in stage IV, the stress saturates at a value of 152 MPa.

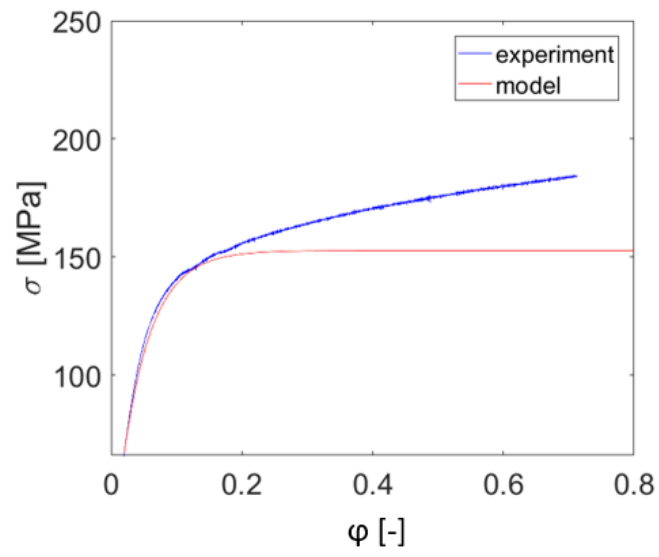


Figure 48: Flow curve obtained by experiments (blue) and determined by the Kocks-Mecking model (red)

7 Summary and Conclusion

An AA6061 aluminium alloy is cold deformed to two final deformation states of $\varphi = 0.4$ and $\varphi = 0.7$ and subsequently recovery annealed at a temperature of 325 °C. The dislocation substructure evolution during cold deformation is observed by using EBSD and is in good agreement with previous investigations [14, 15, 16, 32]. Cell-bands are formed, delineated by Geometrically Necessary Boundaries (GNBs). With increasing strain, the average misorientation between adjacent cell-bands increases, whereas the width of cell-bands decreases. No identification of individual cells is possible in the obtained orientation maps, but according to the similitude principle, which relates the density of dislocations to the average length of a virtual uniform dislocation microstructure [27], the spacing between GNBs is sufficient. By varying the annealing times between 5 seconds and 10^4 seconds, the dislocation evolution during static recovery is investigated. An increasing subgrain size is accompanied by an increasing average misorientation, but a reduction of the total length of GNBs can be observed. These results are in good accordance with T. Furu et al. [23], explaining these results with local strain gradients. A relation between subgrain size and the dislocation density is given by the similitude principle [27]. As a consequence, the decrease of dislocation density during static recovery can be calculated by microstructural investigations. These results fit to those values predicted by the Kocks-Mecking model. The softening behaviour during static recovery is characterized by Brinell hardness tests, but inhomogeneous compression over the specimens' cross section occurred, resulting in a deformation cross. Uneven deformation states can probably be reduced by more applicable lubricants than Graphite and Molybdenum, to minimize friction effects. However, hardness tests in combination with EBSD analysis are a good method for characterizing the influence of recrystallization. Though a sufficient preparation for microstructural investigation was achieved, some scratches and pores are visible on the specimens' surfaces. Even if the preparation method was improved over time, clean up methods and filters are necessary for indexing Kikuchi bands of EBSD patterns and to optimize the confidence indexes.

All in all, measuring the subgrain size and the average misorientation of GNBs during static recovery is an appropriate method for describing the dislocation density evolution and is in good agreement with predicted values of the extended Kocks-Mecking model.

8 References

- [1] W. Demtröder, *Experimentalphysik 3: Atome, Moleküle und Festkörper*. Springer Verlag, 2010.
- [2] A. Kelly and K. M. Knowles, *Crystallography and Crystal Defects*. John Wiley & Sons, Ltd, 2012.
- [3] D. Hull and D. J. Bacon, *Introduction to Dislocations*, Fifth Edit. Elsevier Ltd, 2011.
- [4] W. D. Callister and D. G. Rethwisch, *Materials Science and Engineering*. John Wiley & Sons Ltd, 2011.
- [5] A. H. Cottrell, "Dislocations and Plastic Flow in Crystals," *Am. J. Phys.*, vol. 22(4), pp. 242–243, 1954.
- [6] G. Gottstein, *Physikalische Grundlagen der Materialkunde*. Springer-Verlag, 2007.
- [7] F. Roters, D. Raabe, and G. Gottstein, "Work hardening in heterogeneous alloys—a microstructural approach based on three internal state Variables," *Acta mater*, vol. 48, pp. 4181–4189, 2000.
- [8] P. Lejcek, *Grain Boundary Segregation in Metals*. Springer, 2010.
- [9] F. J. Humphreys, "Characterisation of fine-scale microstructures by electron backscatter diffraction (EBSD)," *Scr. Mater.*, vol. 51, pp. 771–776, 2004.
- [10] F. J. Humphreys, "Reconstruction of grains and subgrains from electron backscatter diffraction maps," *J. Microsc.*, vol. 213, no. 3, pp. 247–256, 2004.
- [11] R. A. Schwarzer, "Automated Crystal Lattice Orientation Mapping Using a Computer-controlled SEM," *Micron*, vol. 28, no. 3, pp. 249–265, 1997.
- [12] A. J. Schwartz, M. Kumar, and B. L. Adams, *Electron Backscatter Diffraction in Materials Science*, Second Edi. Springer, 2009.
- [13] B. Bay, N. Hansen, and D. Kuhlmann-Wilsdorf, "Deformation structures in lightly rolled pure aluminium," *Mater. Sci. Eng. A*, vol. 113, no. C, pp. 385–397, 1989.
- [14] D. A. Hughes, N. Hansen, and D. J. Bammann, "Geometrically necessary boundaries,

- incidental dislocation boundaries and geometrically necessary dislocations,” *Scr. Mater.*, vol. 48, no. 2, pp. 147–153, 2003.
- [15] N. Hansen, “Deformation microstructures,” *Scr. Metall. Mater.*, vol. 27, no. 11, pp. 1447–1452, 1992.
- [16] N. Hansen, “Cold Deformation Structures,” *Mater. Sci. Technol.*, vol. 6, pp. 1039–1047, 1990.
- [17] P. J. Hurley and F. J. Humphreys, “The application of EBSD to the study of substructural development in a cold rolled single-phase aluminium alloy,” *Acta Mater.*, vol. 51, no. 4, pp. 1087–1102, 2003.
- [18] Q. Liu and N. Hansen, “Geometrically necessary boundaries and incidental dislocation boundaries formed during cold deformation,” *Scr. Metall. Mater.*, vol. 32, no. 8, pp. 1289–1295, 1995.
- [19] K. Lücke, “Erscheinungsformen und Ursachen der Rekristallisation der Metalle,” in *Rekristallisation metallischer Werkstoffe*, VEB Deutscher Verlag für Grundstoffindustrie, 1965, pp. 10–38.
- [20] H. Hornbogen, G. Eggeler, and E. Werner, *Werkstoffe: Aufbau und Eigenschaften*. Springer, 2008.
- [21] F. J. Humphreys and M. Hatherley, *Recrystallization and related annealing phenomena*. Elsevier Ltd, 2004.
- [22] O. Ryen, “Work Hardening and Mechanical Anisotropy of Aluminium Sheets and Profiles,” *PhD Thesis Trondheim*, 2003.
- [23] T. Furu, R. Orsund, and E. Nes, “Subgrain Growth in Heavily Deformed Aluminum- Experimental Investigation and Modelling Treatment,” *Acta Metall. Mater.*, vol. 43, no. 6, pp. 2209–2232, 1995.
- [24] Y. Huang and F. J. Humphreys, “Subgrain Growth and Low Angle Boundary,” vol. 48, no. 2000, pp. 2017–2030, 2000.
- [25] H. S. Valberg, “FEA of Metal Forming,” in *Applied Metal Forming: Including FEM Analysis*, Cambridge University Press, 2017, pp. 34–52.

- [26] E. Nes, "Modelling of work hardening and stress saturation in FCC metals," *Prog. Mater. Sci.*, vol. 41, no. 3, pp. 129–193, 1997.
- [27] M. Sauzay and L. P. Kubin, "Scaling laws for dislocation microstructures in monotonic and cyclic deformation of fcc metals," *Prog. Mater. Sci.*, vol. 56, no. 6, pp. 725–784, 2011.
- [28] D. Kuhlmann-Wilsdorf, "LEDs - Properties and Effects of Low Energy Dislocation Structures," *Int. Conf. Low Energy Dislocation Struct.*, pp. 53–66, 1986.
- [29] N. Hansen and C. Y. Barlow, "Plastic Deformation of Metals and Alloys," in *Physical Metallurgy*, Fifth Edit., Elsevier, 2014, pp. 1681–1764.
- [30] U. Kocks and H. Mecking, "Physics and phenomenology of strainhardening: the FCC case," *Prog. Mater. Sci.*, vol. 48, pp. 171–273, 2003.
- [31] E. Kozeschnik, "MatCalc," *Solid state and precipitation kinetics simulation software*, 2017. [Online]. Available: <http://matcalc.tuwien.ac.at/> . [Accessed: 10-Feb-2017].
- [32] E. Povoden-Karadeniz, "MatCalc Thermodynamic Database," "*mc_al.tdb*," 2017. [Online]. Available: <http://matcalc.tuwien.ac.at/index.php/databases/open-databases> . [Accessed: 10-Feb-2017].
- [33] E. Povoden-Karadeniz, "MatCalc Diffusion Database," "*mc_al.ddb*," 2017. [Online]. Available: <http://matcalc.tuwien.ac.at/index.php/databases/open-databases> . [Accessed: 10-Feb-2017].
- [34] "Open database license," *ODbL*. [Online]. Available: <https://opendatacommons.org/licenses/odbl/1.0/> . [Accessed: 10-Feb-2017].
- [35] D. Sparber, "Dislocation substructure evolution of an Al-6016-T4 alloy during cold deformation," *Master Thesis, Tech. Univ. Vienna*, 2016.
- [36] L. Delannay, O. V. Mishin, D. J. Jensen, and P. Van Houtte, "Quantitative analysis of grain subdivision in cold rolled aluminium," *Acta Mater.*, vol. 49, no. 13, pp. 2441–2451, 2001.
- [37] P. J. Hurley, P. S. Bate, and F. J. Humphreys, "An objective study of substructural boundary alignment in aluminium," *Acta Mater.*, vol. 51, no. 16, pp. 4737–4750, 2003.

- [38] P. J. Hurley and F. J. Humphreys, "Characterizing the deformed state in Al-0.1 Mg alloy using high-resolution electron backscattered diffraction," *J. Microsc.*, vol. 205, pp. 218–225, 2002.
- [39] Y. Huang, F. J. Humphreys, and M. Ferry, "The annealing behaviour of deformed cube-oriented aluminium single crystals," *Acta mater*, vol. 48, pp. 2543–2556, 2000.

9 List of figures

Figure 1: Unit cell with basis vectors a , b and c [3]	4
Figure 2: Lattice plane intersecting the coordinate system	5
Figure 3: Additional half-plane of atoms causing an edge dislocation; a is the atomic distance [4]	6
Figure 4: (a) Burgers circuit in a perfect lattice; (b) lattice with an included half-plane; b defines the Burgers vector [4]	7
Figure 5: Screw dislocation [4]	7
Figure 6: Misorientation based on edge dislocation; b is the Burgers vector, D the dislocation spacing [8]	9
Figure 7: (a) Scheme of EBSD measurements [11]; (b) obtained Kikuchi bands [6]	10
Figure 8: Point P indicates a crystallographic plane's orientation by a point on the surface of a sphere and P' is the stereographic projection onto a plane [12]	11
Figure 9: (a) EBSD map showing a typical substructure after 50% rolling of a high purity Al–0.13 wt% Mg DC cast alloy [17]; (b) schematic representation of cell-blocks within a grain [16]	12
Figure 10: Transmission electron micrograph of deformed pure Ni; delineation of GNBs, IDBs and the rolling direction [14]	13
Figure 11: Cells within a grain subdivided by MBs [16]	13
Figure 12: (a) Spacings [22] and (b) misorientation of GNBs and IDBs as function of strain [14]	15
Figure 13: (a) Subgrain size as a function of annealing time; (b) misorientation as a function of annealing time	16
Figure 14: Rate of grain boundary growth per unit volume S_V for different modes of deformation [21]	17
Figure 15: FEM-predicted distribution of effective strain in hot compression of Al cylinder [25]	18
Figure 16: (a) Flow curve subdivided into stage II, stage III and stage IV; (b) Kocks-Mecking diagram visualizing strain hardening (θ) vs flow stress (τ) [26]	19
Figure 17: Description of σ_0 , θ_0 and σ_∞ for an unambiguous definition of a flow curve	21
Figure 18: AA6061 plate	23
Figure 19: Dimension [mm] of the cylindrical specimen	23
Figure 20: Scheme of heat treatment process	24
Figure 21: Schematic structure of Gleeble 1500; F: applied force; 1: tungsten stamps; 2: specimen; 3: molybdenum foil; 4: graphite foil	25

Figure 22: Schematic array for hardness tests	27
Figure 23: Screenshot of the settings, defining a grain in OIM.....	29
Figure 24: Guidance how adjust the settings to create a Kernel Misorientation map.....	29
Figure 25: Clean up types including the clean up parameters, which can be selected by the user.....	30
Figure 26: Grain dilation.....	31
Figure 27: Misorientation measurement perpendicular to cell bands; peaks higher 4° characterize GNBs	31
Figure 28: MatCalc simulation of the phase fraction of GP-zones, β'' and β' precipitates for the adjusted heat treatment.....	32
Figure 29: Brinell hardness values as function of the annealing time for both deformation states of (a) $\varphi = 0.4$ and (b) $\varphi = 0.7$. For each annealing time, seven tests are performed on different positions along the specimen's centreline	33
Figure 30: Softening behaviour of both deformation states ($\varphi = 0.4$ and $\varphi = 0.7$)	34
Figure 31: Deformation to a final strain of $\varphi = 0.7$, without subsequent annealing process; (b) is an enlargement of the rectangle A in (a) including GNBs with misorientations higher 4°, marked as red lines	35
Figure 32: (a) Misorientation measurement perpendicular to cell bands; peaks higher 4° characterize GNBs; (b) histogram of the spacings of GNBs	36
Figure 33: (a) Microstructure after a deformation to a final true strain $\varphi = 0.7$ with subsequent annealing for 150 seconds at 325 °C; (b) enlargement of rectangle A in (a), red lines indicate GNBs.....	37
Figure 34: (a) Misorientation measurement perpendicular to cell bands; peaks higher 4° characterize GNBs; (b) histogram of the spacings of GNBs	37
Figure 35: (a) Microstructure after a deformation to a final true strain $\varphi = 0.7$ with subsequent annealing for 700 seconds at 325 °C; (b) and (c) show enlargements of both rectangles A and B, red lines indicate GNBs	38
Figure 36: (a) Histogram of the spacings of GNBs after annealing for 700 seconds; (b) misorientation measurement after a deformation to a final strain of $\varphi = 0.7$ and subsequent annealing for 700 seconds at 325 °C.....	39
Figure 37: Deformation to a final strain of $\varphi = 0.4$, without subsequent annealing process; (b) is an enlargement of the rectangle in (a), including GNBs with misorientations higher 4°, marked as red lines	39
Figure 38: (a) Misorientation measurement; (b) histogram of the spacings of GNBs.....	40
Figure 39: Deformation to a final strain of $\varphi = 0.4$, with subsequent annealing for 700 seconds at 325 °C (b) is an enlargement of the rectangle A in (a) including GNBs with misorientations higher 4°, marked as red lines	41

Figure 40: (a) Misorientation measurement after a deformation to a final strain of $\varphi = 0.4$ and subsequent annealing for 3.000 seconds at 325 °C; (b) histogram of the spacings of GNBs after annealing for 700 seconds.....	41
Figure 41: Deformation to a final strain of $\varphi = 0.4$, with subsequent annealing for 10.000 seconds at 325 °C; (b) is an enlargement of the rectangle in (a) including GNBs with misorientations higher 4°, marked as red lines	42
Figure 42: (a) Misorientation measurement after a deformation to a final strain of $\varphi = 0.4$ and subsequent annealing for 10.000 seconds at 325 °C; (b) histogram of the spacings of GNBs	43
Figure 43: Misorientation (a) and subgrain size (b) as a function of the annealing-time at 325°C; considering two deformation states: $\varphi = 0.4$ and $\varphi = 0.7$	43
Figure 44: Misorientation as a function of the grain size (a); length of GNBs as a function of annealing time for the deformation states $\varphi = 0.4$ and $\varphi = 0.7$ (b).....	44
Figure 45: (a) Hardness values as a function of annealing time: experimental results at an annealing temperature of 325 °C; (b) cold rolled ($\varepsilon = 1$) Al0.43 wt% Fe0.09 wt% Si alloys for a range of annealing temperatures	45
Figure 46: Dislocation density (ρ) as a function of annealing time (t) at 325 °C; solid lines are modelled by the extended Kocks-Mecking approach; stars and triangles ($\varphi = 0.4$ and $\varphi = 0.7$) are calculated by experimental values and the similitude principle; crosses are calculated with the Taylor relation	47
Figure 47: (a) Flow curves to final strains of $\varphi = 0.4$ and $\varphi = 0.7$; (b) Kocks-plot: blue: slope (θ) of the stress-strain curve as a function of σ [MPa], red: linear approximation of stage III	48
Figure 48: Flow curve obtained by experiments (blue) and determined by the Kocks-Mecking model (red).....	49
Figure 49: Kernel Average Misorientation (KAM) maps of deformed specimen to $\varphi = 0.7$, (a) without subsequent annealing, (b) after 150 seconds, (c) after annealing for 700 seconds; each colour indicates a local misorientation angle as shown below the maps.....	60
Figure 50: Kernel Average Misorientation (KAM) maps of deformed specimen to $\varphi = 0.4$, (a) without subsequent annealing, (b) after 3.000 seconds, (c) after annealing for 10.000 seconds; each colour indicates a local misorientation angle as shown below the maps.....	61
Figure 51: Passing area of a dislocation; d_{crit} is the annihilation distance between two dislocations.....	62

10 List of tables

Table 1: Chemical composition in wt% of AA6061 alloys.....	23
Table 2: Calculated Gleeble input parameters.....	26
Table 3: Annealing times for compressed specimens to $\varphi = 0.4$ and $\varphi = 0.7$	26
Table 4: Polishing and grinding steps [35].....	28
Table 5: Subgrain characterization of the deformation state of $\varphi = 0.4$	44
Table 6: Subgrain characterization of the deformation state of $\varphi = 0.7$	44
Table 7: Influence of increasing deformation and annealing time on misorientation, subgrain size and the length of GNBs	46

11 Appendix

Nomenclature

EBSD	electron backscatter diffraction
OIM	orientation imaging microscopy
G	shear modulus [MPa]
M	taylor factor [-]
α	strengthening coefficient [-]
fcc	face centre cubic
b	burgers vector
T	temperature [°C]
t	time [s]
θ	misorientation [°]
$\dot{\theta}$	work hardening rate [MPa]
Γ	line energy of a dislocation [J/m]
F	deformation force [N]
ρ	dislocation density [m/m^3]
σ	stress [MPa]
ϵ	engineering strain [-]
γ	shear strain [-]
A	fitting parameter
B	fitting parameter
φ	true strain [-]
$\dot{\varphi}$	strain rate [s^{-1}]
γ_{SFE}	stacking fault energy [J/m^2]
δ	distance between GNBs [m]
τ	shear stress [N/mm^2]
d_0	initial sample diameter [m]
h_0	initial sample length [m]

DDW_____dense dislocation wall
 MB_____microband
 GNB_____geometrical necessary boundary
 IDB_____incidental dislocation boundary
 SEM_____scanning electron microscopy
 TEM_____transmission electron microscopy
 KAM_____kernel average misorientation
 RD_____rolling direction
 TD_____transverse direction
 ND_____normal direction

Results EBSD

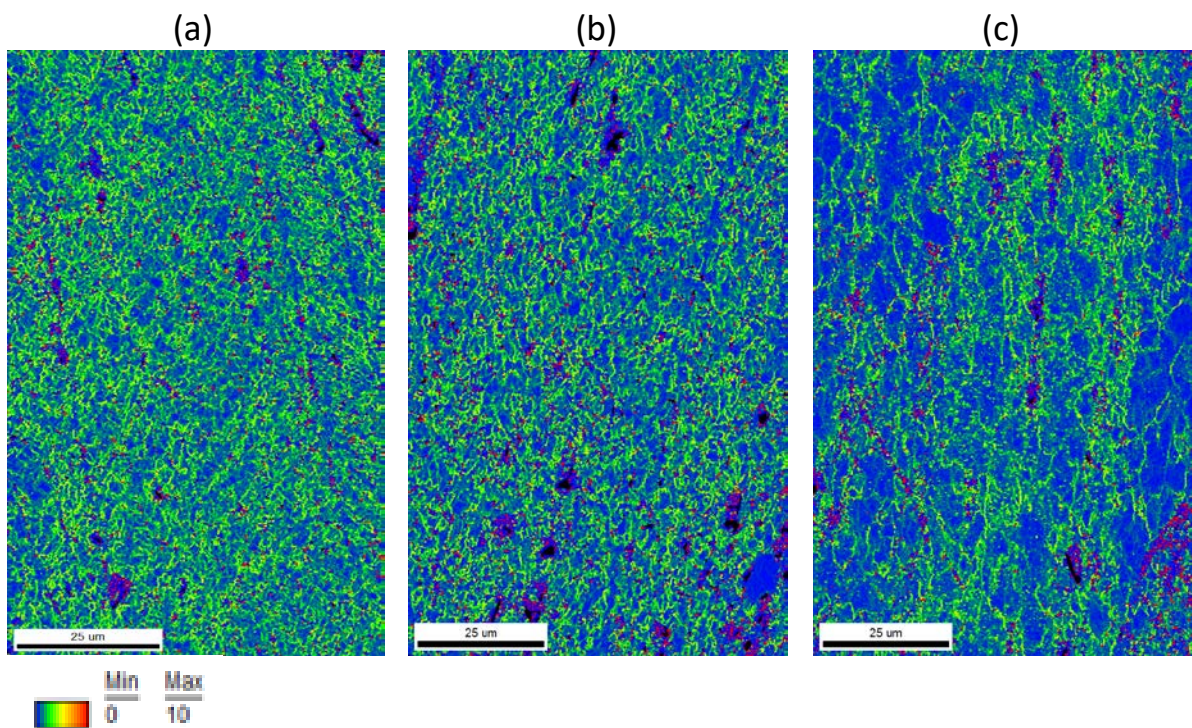


Figure 49: Kernel Average Misorientation (KAM) maps of deformed specimen to $\phi = 0.7$, (a) without subsequent annealing, (b) after 150 seconds, (c) after annealing for 700 seconds; each colour indicates a local misorientation angle as shown below the maps

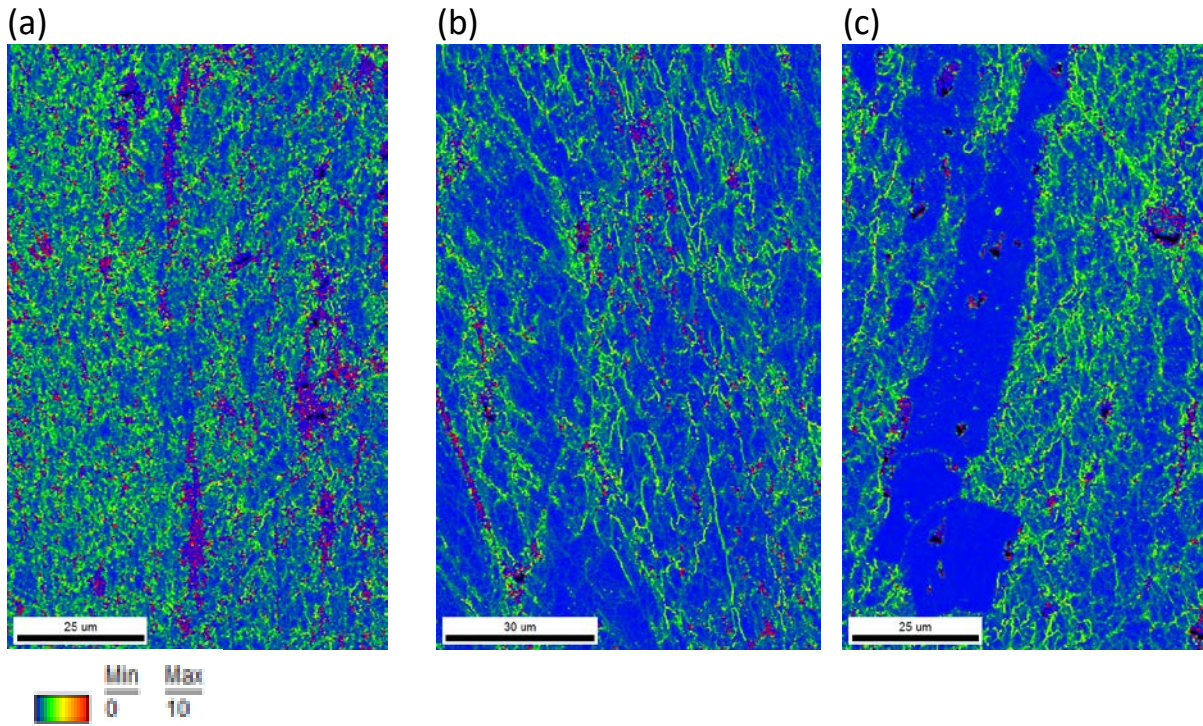


Figure 50: Kernel Average Misorientation (KAM) maps of deformed specimen to $\phi = 0.4$, (a) without subsequent annealing, (b) after 3.000 seconds, (c) after annealing for 10.000 seconds; each colour indicates a local misorientation angle as shown below the maps

Derivation of $d\rho^+/d\gamma$ and $d\rho^-/d\gamma$

The proportional factor A refers to the immobile dislocation production, when dislocations get stuck in front of an obstacle after moving a distance λ (mean free path). The increase of dislocation density is:

$$\frac{d\rho^+}{\rho_m} = \frac{dx}{\lambda} \quad (21)$$

The total dislocation density increases by ρ_m , if the moving distance dx is equal λ . Using the Orowan equation

$$\dot{\gamma} = \rho_m * b * v \rightarrow d\gamma = \rho_m * b * dx \quad (22)$$

leads to:

$$\frac{d\rho^+}{\rho_m} = \frac{d\gamma}{\lambda * \rho_m * b} \rightarrow \frac{d\rho^+}{d\gamma} = \frac{1}{\lambda * b} \quad (23)$$

With increasing dislocation density ρ , the mean free path decreases:

$$\lambda = \frac{A}{\sqrt{\rho}} \rightarrow \frac{d\rho^+}{d\gamma} = \frac{\sqrt{\rho}}{A*b} \rightarrow \frac{d\rho^+}{d\varepsilon} = \frac{M}{A*b} \sqrt{\rho} \quad (24)$$

Factor B describes dynamic recovery at low and intermediate temperatures. Annihilation occurs when two dislocations of opposite sign get closer than d_{crit} . A moving dislocation on a glide plane travels the distance $v * dt$, and passes the area $A = v * dt * 2 * d_{crit}$, as indicated in Figure 51 [7].

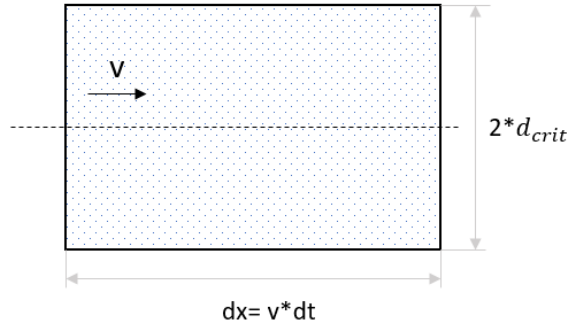


Figure 51: Passing area of a dislocation; d_{crit} is the annihilation distance between two dislocations

The reaction rate for annihilation yields:

$$\frac{dp}{dt} = v * 2 * d_{crit} * \rho * B, \quad (25)$$

Multiplied with the density of moving dislocations ρ_m , using the Orowan Eq. (22), and the relation $\dot{\gamma} = M * \varepsilon$, leads to:

$$\frac{d\rho^-}{dt} = 2 * d_{crit} * \rho * B * \rho_m * \frac{\dot{\gamma}}{\rho_m * b} \rightarrow \frac{d\rho^-}{d\varepsilon} = 2 * d_{crit} * \rho * B * \frac{M}{b} \quad (26)$$